



3D CFD-PBM Modeling of Industrial Fluidized Bed Polymerization Reactor for Polyethylene Production

Catarina de Oliveira Reis

Thesis to obtain a Master of Science Degree in

Chemical Engineering

Supervisors: Professor Vítor Manuel Geraldês Fernandes

Professor Pornchai Bumroongsri

Examination Committee

Chairperson: Professor Carlos Henriques

Supervisor: Professor Vítor Geraldês

Members of the Committee: Professor Sebastião Alves

October 2019



Mahidol University
Wisdom of the Land

This work was developed in Mahidol University- Faculty of engineering
Bangkok, Thailand

*“This is presented as a work of fiction
and dedicated to nobody”*

Charles Bukowski

Acknowledgments

First, I would like to thank my main and sole sponsor, *Reis Family*. I wanted to thank you for not giving up on me and for thinking that I was a good investment for your money. At least I'm better than BES. However, it should be noted that my sister made no monetary contribution to this. I would also like to thank you for adapting to all of this and always being present, even with a mostly absent daughter. Thank you for not imposing obstacles on my crazy idea of going to Bangkok. It was undoubtedly the experience of my life.

Secondly, I want to thank my *boyfriend* and congratulate him on not going crazy after these five years. The person who showed me the other side of academic life in the student's city, Coimbra. The person who taught me to breathe and made me see that this is just a course, just a dissertation, and just a phase of my life. To enjoy what is good and accept the rest. Finally, thank you for being crazy enough to meet me on the other side of the world.

Thirdly I would like to thank Margarida and Tita. The friends who listened to me, helped, advised, supported, and above all, they were always sincere to me. That made me see that my ambitions were not dreams, but that I could achieve them.

Fourthly, I would like to thank the people I carry in my heart. Thank you for having suffered with me. It made everything so much more enjoyable and endurable. Together we have created a wailing wall, and we did not sleep whole nights studying or drinking. Together we accepted our status as Técnico students, deprived of a healthy social life, and had the best years. Thank you *Freshman of Truth, Dercio, Dobby, Male Wine Barrel, Pat, Bowls, Star Fruit, Paiva, Daniela, and Patrícia*.

Fifthly, I would like to thank all the Professors I had the chance to meet during my academic years, and I apologize for not having attended most of the classes. No doubt, if I could go back in time, I would enjoy much more and take out as much knowledge as possible from your shares and experience.

Thanks to Professor Pornchai for guiding me into a wholly unknown and crazy country and showing me the purest thing in Thailand. He was the one that helped me through all the process before coming to Bangkok. He helped me slow down and was tireless in clarifying all my doubts, always with a smile. *Thailand, the country of smiles*.

Thanks to Professor Geraldés for teaching me how to value my work and how to show it. He was super helpful in helping me with everything I needed.

Last but not least, I would like to thank myself, no doubt that I was the crucial element for all this to happen, and if I had given up, you would not have the incredible opportunity to read this dissertation.

Resumo

A presente dissertação tem como objetivo desenvolver um modelo 3D de dinâmica de fluídos computacional (CFD) integrado com o modelo de balanço populacional (PBM), e estudar os padrões de movimento das partículas de polietileno (PE) considerando o crescimento das mesmas num reator de leito fluidizado (FBR) à escala industrial, utilizando o programa ANSYS Fluent 16.

Desenvolveu-se um modelo CFD para estudar o comportamento hidrodinâmico das partículas de PE numa unidade de fluidização à escala piloto, sendo que não se considerou a reação de polimerização. Com este modelo previu-se o movimento das partículas de PE e a perda de pressão.

Com fim a validar o modelo, simulou-se para duas velocidades diferentes: 3.3 m/s e 5.7 m/s ($Re=870$ e $Re=1520$, respetivamente). Relativamente à perda de pressão, os resultados obtidos demonstram consistência entre os dados experimentais obtidos na unidade de fluidização à escala piloto disponível no laboratório da faculdade e o valor teórico. Comparando o valor teórico (5.89 mbar) com o valor experimental (7 mbar) e o resultado da simulação (5.91 mbar), verifica-se um erro associado de 18.9% e 0.3%, respetivamente.

O modelo desenvolvido foi acoplado com o PBM e foi simulado para um FBR escala industrial a uma velocidade de 0.38 m/s ($Re=770$). Verificou-se que o modelo é capaz de representar corretamente o movimento da mistura com uma razoável precisão em relação à perda de pressão o resultado da simulação apresenta um erro de 1.7% relativamente ao valor teórico. Os resultados da simulação mostram ainda que o diâmetro médio das partículas aumenta no decorrer do tempo com uma taxa de crescimento de partículas de 1.62 $\mu\text{m/s}$, obtendo-se um diâmetro médio final de 545,1 μm partindo de um diâmetro médio inicial de 200 μm .

Portanto, o modelo 3D CFD-PBM pode ser usado como uma ferramenta fiável para analisar e melhorar o design e a operação dos FBRs de polimerização em fase gasosa.

Palavras-chave: Polietileno, Dinâmica de fluídos computacional, Modelo de balanço populacional, Reator de leito fluidizado, Fluidização

Abstract

The present dissertation has the objective of developing a three-dimensional (3D) computational fluid dynamics (CFD) model integrated with the population balance model (PBM) and study the polyethylene (PE) particle flow patterns considering particle growth in industrial-scale fluidized bed reactor (FBR), utilizing ANSYS Fluent software 16.

A CFD model was developed to study the cold-flow behavior of PE particles in a pilot-scale FBR, where the polymerization reaction was not considered, and the particle flow behavior and the bed pressure drop of PE particles were predicted.

In order to validate the model, two different velocities were simulated: 3.3 m/s and 5.7 m/s ($Re=870$ and $Re=1520$, respectively). The predicted results reveal an acceptable agreement with the observed experimental data obtained from the faculty laboratory's pilot-scale fluidization unit and theoretical values regarding pressure drop. Comparing the theoretical value (5.89 mbar) with the experimental value (7 mbar) and the simulation result (5.91 mbar), there is an error of 18.9% and 0.3%, respectively.

The developed model was coupled with PBM and performed in an industrial-scale FBR at 0.38 m/s ($Re=770$). The model is able to represent the actual behavior of real mixture with reasonable accuracy with a 1.7% error between simulation result and theoretical value of pressure drop. The simulation results show that through time, the average particle size increase with a particle growth rate of 1.62 $\mu\text{m/s}$, obtaining a final average diameter of 545.1 μm from an initial average diameter of 200 μm .

Hence, the 3D CFD-PBM coupled model can be used as a reliable tool for analyzing and improving the design and operation of the gas phase polymerization FBRs.

Keywords: Polyethylene, Computational fluid dynamics, Population balance model, Fluidized bed reactor, Fluidization

Contents

Acknowledgments	vii
Resumo	ix
Abstract	xi
List of Figures	xv
List of Tables	xix
Nomenclature	xxi
Glossary	xxv
1. INTRODUCTION	1
2. OVERVIEW OF POLYETHYLENE PRODUCTION	5
2.1 Polyethylene	5
2.2 Polyethylene Production	8
2.2.1 Processes Classification	10
2.2.2 Gas-phase reactors.....	13
2.2.3 Kinetic Model.....	16
2.3 Computational Models	18
2.3.1 Computational Fluid Dynamics	18
2.3.2 Population Balance Model	23
2.3.3 Coupling between the CFD two-fluid model and PBM.....	28
3. NUMERICAL METHODS	29
3.1 CFD model- Pilot-scale fluidization unit.....	29
3.1.1 Geometry.....	29
3.1.2 Mesh.....	31
3.1.3 Setup simulation data.....	33
3.2 CFD- PBM coupled model- industrial-scale FBR	35
3.2.1 Geometry	35
3.2.2 Mesh.....	37
3.2.3 Setup simulation data.....	38
4. EXPERIMENTAL METHODS.....	41
4.1 CDF model validation- Pilot-scale fluidization unit.....	41

5. RESULTS	46
5.1 CFD-PBM coupled model	46
6. CONCLUSIONS AND FUTURE WORK	55
7. REFERENCES	57
Appendix A – Particle classification	61
Appendix B – Pilot-scale reactor dimensions	62
Appendix C – Sensitivity analysis of grid	64
C.1. Grid for pilot-scale fluidization unit	64
C.2. Grid for industrial-scale FBR	66
Appendix D – Particle growth rate	68
Appendix E – User Defined Functions	70
E.1. User Defined Function for particle growth rate	70
E.2. User Defined Function for polymerization heat	71

List of Figures

Figure 1- Polyethylene innovations versus time.....	2
Figure 2- Ethylene Production Technologies	2
Figure 3 - Chemical structure of pure polyethylene.	5
Figure 4- Main downstream processes/applications of HDPE in 2017.	6
Figure 5- Main downstream processes/applications of LDPE in 2017.....	6
Figure 6 – General schema of polyolefin production unit using Z-N catalysts.....	8
Figure 7- Unipol process for PE manufacture.	12
Figure 8- Schematic diagram of an industrial fluidized-bed polyethylene reactor.	13
Figure 9-Fluidization regimes	15
Figure 10- The evolution of particle-size distribution in the fluidized-bed olefin polymerization reactor.	24
Figure 11- Particle growth evolution.....	27
Figure 12-CFD-PBM coupled model.	28
Figure 13- Pilot-scale fluidization unit available in the Faculty's laboratory	30
Figure 14-a) pilot-scale fluidization unit geometry b) five bodies of pilot-scale fluidization unit geometry (CFD simulation)	30
Figure 15- Different perspectives of the pilot-scale fluidization unit geometry a) lateral b) top c) bottom (CFD simulation)	31
<i>Figure 16- Mesh for the pilot-scale fluidization unit with 118 557 nodes (CFD simulation)</i>	<i>31</i>
Figure 17- Mesh and boundary conditions for the pilot-scale fluidization unit with 118 557 nodes a) wall b) outlet c) inlet (CFD simulation)	32
Figure 18-a) industrial-scale FBR geometry b) five bodies of industrial-scale FBR geometry ...	36
Figure 19-Different perspectives of the industrial-scale FBR geometry a) lateral b) top c) bottom	36
Figure 20- Mesh for the industrial-scale reactor with 309 551 nodes	37
Figure 21-Mesh and boundary conditions for the industrial-scale reactor with 309 551 nodes a) wall b) outlet c) inlet (CFD-PBM simulation)	37
Figure 22- Initial particle size distribution in the industrial-scale FBR for the CFD-PBM simulation.	40

Figure 23- Amplitude of pressure fluctuation across the bed increases as the bed approaches turbulent fluidization.	42
Figure 24- The particle flow behaviors for three different velocities performed in the faculty laboratory's pilot-scale fluidization unit. a) 0.9 m/s b) 3.3 m/s c) 5.7 m/s.....	43
Figure 25- Simulation results of particle flow behavior compared with experimental particle flow behavior in the laboratory's pilot-scale fluidization, both at 3.3 m/s.....	44
Figure 26- Results of particle flow behavior compared with experimental particle flow behavior in the laboratory's pilot-scale fluidization unit, both at 5.7 m/s.....	45
Figure 27- Transient fluidization. Pressure drop in function of time in an industrial-scale FBR with a CFD-PBM simulation. Classical value of 0.4153(CFD simulation) <i>bar</i> from classical equation (1) and (2), calculated in C.2. Grid for industrial-scale FBR	46
Figure 28- Volume rendering of gas velocity in an industrial-scale FBR with a CFD-PBM simulation.	47
Figure 29 - The evolution of solid volume fraction contour in an industrial-scale FBR with a CFD-PBM simulation.....	48
Figure 30- The time-averaged solid velocity for each plan along the bed height in an industrial-scale FBR with a CFD-PBM simulation.....	49
Figure 31- The time-averaged solid volume fraction for each plan along the bed height in an industrial-scale FBR with a CFD-PBM simulation.	49
Figure 32-The particle velocity profile along the radial direction (a) and the mean solid volume fraction along the radial direction(b) at 250 s in an industrial-scale FBR with a CFD-PBM simulation.	50
Figure 33- The evolution of solid volume fraction contour in the reactor for different heights in an industrial-scale FBR with a CFD-PBM simulation.	50
Figure 34- The evolution of solids temperature contour in an industrial-scale FBR with a CFD-PBM simulation.....	51
Figure 35- The time-averaged solids temperature along the bed height in an industrial-scale FBR with a CFD-PBM simulation.	51
Figure 36- Solids temperature profile along the radial direction at 250 s in an industrial-scale FBR with a CFD-PBM simulation.	52
Figure 37- The particle size distribution due to the growth rate in an industrial-scale FBR with a CFD-PBM simulation.	53
Figure 38-Powder classification of granular solids.	61
Figure 39- Design of the pilot-scale reactor provided by the manufacture	62

Figure 40- Design of the pilot-scale reactor provided by the manufacture 63

Figure 41-The pressure drop as a function of flow time using different grids in a pilot-scale fluidization unit with a CFD simulation. ($v_g=3.3$ m/s). The theoretical value of 5.89 mbar from classical equation (1) and (2), and the experimental value of 7 mbar from the experiment in the laboratory's pilot-scale fluidization unit..... 64

Figure 42- The pressure drop as a function of bed height using different grids in a pilot-scale fluidization unit with a CFD simulation. ($v_g=3.3$ m/s, $t=30$ s) 65

Figure 43- The pressure drop as a function of flow time using different grids in an industrial-scale FBR with a CFD-PBM simulation. ($v_g=0.38$ m/s). The theoretical value of 0.4153 bar from classical equations (1) and (2). 66

Figure 44- The pressure drop as a function of bed height using different grids in an industrial-scale FBR with a CFD-PBM simulation. ($v_g=0.38$ m/s, $t=50$ s) 67

Figure 45-Predicted average particle diameter times profile in the industrial FBR in CFD-PBM simulation. 69

List of Tables

Table 1- Summary of the properties of PE.....	7
Table 2- Examples of uses of PE.....	7
Table 3- Elementary reactions and rate constants of PE polymerization process.....	17
Table 4- Number of nodes and quality parameters for the pilot-scale fluidization unit meshes..	32
Table 5- Boundary conditions and model parameters for CFD model simulation in a pilot-scale fluidization unit.....	33
Table 6- Physical properties of gas and solid phases for CFD model simulation in a pilot-scale fluidization unit.....	33
Table 7-Number of nodes and quality parameters for the industrial-scale reactor meshes	38
Table 8- Physical properties of gas and solid phases for CFD-PBM model simulation in an industrial-scale FBR	38
Table 9- Kinetic parameters for CFD-PBM model simulation in an industrial-scale FBR	39
Table 10- Boundary conditions and model parameters for CFD-PBM model simulation in an industrial-scale FBR	39
Table 11- Particles classification	61
Table 12- Grid analysis for pilot-scale fluidization unit with a CFD simulation.....	65
Table 13- Grid analysis for industrial-scale	67
Table 14- Average particle diameter in function of time.....	68

Nomenclature

$AlEt_3$	Triethyl aluminum co-catalyst	-
$[C]$	Active catalyst site concentration	mol/m^3
$C_\mu, C_{1\varepsilon}, C_{2\varepsilon}$	Coefficients in turbulence model	-
C_D	Drag Coefficient	-
$C_{p,g}$	Heat capacity coefficient of gas phase	$J/(kg \cdot K)$
$C_{p,i}$	Heat capacity coefficient of i^{th} phase	$J/(kg \cdot K)$
$C_{p,s}$	Heat capacity coefficient of solid phase	$J/(kg \cdot K)$
d_s	Particle diameter	m
e_s	Particle-particle restitution coefficient	-
e_w	Particle-wall restitution coefficient	-
E_a	Activation energy of ethylene polymerization	J/mol
g	Gravitational acceleration	m/s^2
g_0	Radial distribution function	-
G	Particle growth rate	m/s
$G_{k,m}$	Production of turbulent kinetic energy	-
ΔH	Polymerization heat capacity	kJ/mol
H	Bed height	m
h_g	Specific enthalpy of gas phase	$J/(kg \cdot K)$
h_s	Specific enthalpy of solid phase	$J/(kg \cdot K)$
h_{gs}	Heat transfer coefficient of gas to solid phase	$W/(K \cdot m^3)$
h_{sg}	Heat transfer coefficient of solid to gas phase	$W/(K \cdot m^3)$
\bar{I}	Identity matrix	-
I_{2D}	Second invariant of the deviatoric stress tensor	-
K_{sg}	Interphase exchange coefficient	$(kg \cdot m^2)/s$
κ	Turbulence kinetic energy tensor	-
k_p	Propagation rate related to the temperature of particle	$m^3/(mol \cdot s)$
k_p^0	Frequency factor of propagation reaction	$m^3/(mol \cdot s)$
k_{gs}	Diffusion coefficient for granular energy	-
$k_f(j)$	Formation rate constant for a site of type j	-

$k_{i_j}(j)$	Rate constant for initiation of a site of type j by monomer M_i	-
$k_{p_{ik}}(j)$	Propagation rate constant for a site of type j with terminal monomer M_i reacting with monomer M_k	-
$k_{f_{mik}}(j)$	Transfer rate constant for a site of type j with terminal monomer M_i reacting with monomer M_k	-
$k_{dI}(j)$	Deactivation by impurities rate constant for a site of type j	-
$k_{fh_i}(j)$	Transfer rate constant for a site of type j with terminal monomer M_i reacting with hydrogen	-
$k_{h_i}(j)$	Rate constant for reinitiating of a site of type j by monomer M_i	-
$k_{h_r}(j)$	Rate constant for reinitiating of a site of type j by cocatalyst	-
$k_{fr_i}(j)$	Transfer rate constant for a site of type j with terminal monomer M_i reacting with $AlEt_3$	-
$k_{fs_i}(j)$	Spontaneous transfer rate constant for a site of type j with terminal monomer M_i	-
$k_{ds}(j)$	Spontaneous deactivation rate constant for a site of type j	-
L_0	Initial particle diameter	m
L_i	Particle diameter	m
$[M]$	Monomer concentration	mol/m^3
\dot{m}_{sg}	Interphase mass transfer rate of solid to gas phase	$kg/(s \cdot m^3)$
\dot{m}_{gs}	Interphase mass transfer rate of gas to solid phase	$kg/(s \cdot m^3)$
Nu_s	Nusselt number of solid phase	-
$N^*(j)$	Potential active site of type j	-
$N(0, j)$	Uninitiated site of type j produced by formation reaction	-
$N_i(r, j)$	Living polymer molecule of length r, growing at an active site of type j, with terminal monomer M	-
$N_d(j)$	Spontaneously deactivated site of type j	-
$N_{dIH}(0, j)$	Impurity killed sites of type j	-
p	Pressure	Pa
p_g	Gas phase pressure	Pa
p_s	Solid phase pressure	Pa
Pr	Prandtl number	-

q_g	Heat flux of gas phase	W/m^2
q_s	Heat flux of solid phase	W/m^2
Q_{gs}	Intensity of heat exchange between gas and solid phase	$W/(s \cdot m^3)$
Q_{sg}	Intensity of heat exchange between solid and gas phase	$W/(s \cdot m^3)$
$Q_{rs\alpha}$	Heat produced from polymerization reaction	kJ/mol
$Q(r, j)$	Dead polymer molecule of length r produced at a site of type j	-
R	Gas constant	$J/(mol \cdot K)$
R_p	Reaction rate	$mol/(m^3 \cdot s)$
Re_s	Particles Reynolds number	-
t	Flow time	s
T	Temperature	K
T_g	Gas temperature	K
T_s	Solid temperature	K
u_{mf}	Minimum fluidization velocity	m/s
u_t	Particle terminal velocity	m/s
v_g	Gas velocity	m/s
v_s	Solid velocity	m/s
v'_s	Fluctuating particle velocity	m/s

Greek symbols

α_g	Volume fraction of gas phase	-
α_s	Volume fraction of solid phase	-
α_k	Inverse effective Prandtl numbers	-
α_ε	Inverse effective Prandtl numbers	-
$\alpha_{s,max}$	Maximum volume fraction of the solid phase	-
θ_s	Granular temperature	m^2/s^2
μ_g	Viscosity of gas phase	$kg/(m \cdot s)$
μ_s	Viscosity of solid phase	$kg/(m \cdot s)$
$\mu_{s,kin}$	Solid kinetic viscosity	$Pa \cdot s$
$\mu_{s,col}$	Solid collisional viscosity	$Pa \cdot s$
$\mu_{s,fr}$	Solid frictional viscosity	$Pa \cdot s$

$\mu_{t,m}$	Frictional viscosity of system the mixture phase	$Pa \cdot s$
ρ_g	Density of gas phase	kg/m^3
ρ_s	Density of solid phase	kg/m^3
ρ_m	Density of mixture	kg/m^3
$\bar{\tau}_g$	Shear stress of gas phase	N/m^2
$\bar{\tau}_s$	Shear stress of solid phase	N/m^2
λ_s	Solid bulk viscosity	$kg/(m \cdot s)$
ε_s	Turbulence dissipation rate	m^2/s^3
ε	Void fraction	-
κ_s	Thermal conductivity of solid phase	$W/(m \cdot K)$
κ_g	Thermal conductivity of gas phase	$W/(m \cdot K)$
γ_{θ_s}	Collision dissipation of energy	m^2/s^2
φ_{gs}	Exchange of fluctuating energy between two phases	-
Φ_{gs}	The dissipation of granular energy resulting from the Fluctuating forcer	m^2/s^2

Glossary

PE	Polyethylene
LDPE	Low density polyethylene
HDPE	High density polyethylene
LLDPE	Linear low density polyethylene
Z-N	Ziegler-Natta
PSD	Particle size distribution
CFD	Computational fluid dynamics
FBR	Fluidized bed reactor
PBM	Populace balance model
MI	Melt flow index
VSBR	Vertical stirred bed reactor
HSBR	Horizontal stirred bed reactor
MZCR	Multizone circulating reactor
TMA	Trimethylaluminum
TEA	Triethyl aluminium
DEAC	Diethyl aluminum chloride
KTFG	Kinetic theory of granular flow
RNS	Reynolds averaged Navier-stokes
SMM	Standard method of moments
QMOM	Quadrature method of moments
DQMOM	Direct Quadrature Method of Moments
NDF	Length number density

1. INTRODUCTION

Polyethylene (PE) is a thermoplastic polymer with a variable crystalline structure, and it has the simplest basic structure of any polymer. Polymerizing the gas ethylene, C_2H_4 , used as a monomer, is obtained PE. [1] Due to the great versatility of the physical and chemical properties of PE, and to the fact that it can be produced using various technologies with a wide range of possible uses, PE is one of the most widely produced plastics in the world.

The global production capacity was around 113 million metric tonnes in 2017, and the global production capacity increase is expected, being approximately 133 million metric tons in 2022 with an annual growth rate of 3%. [2]

Commercially, PE is produced from ethylene and was accidentally discovered in 1933, while researching ethylene reactions at high temperatures and pressures by Imperial Chemical Company. The first high-pressure low density polyethylene (LDPE) commercial plant was built by ICI in 1939 using an autoclave reactor and, subsequently, BASF developed a tubular reactor for the high-pressure LDPE process. [3]

However, in 1953, two other routes were developed and introduced. The first one, using a transition metal compound in combination with aluminum alkyls or similar materials, Ziegler-Natta (Z-N) catalyst, and the second one using silica/alumina-supported chromium oxide catalyst, Phillips process. These two routes allowed PE production at lower temperatures and pressures, and production of polymer with a modified structure, high-density polyethylene (HDPE). In the years that followed, the efficiency of the Z-N catalyst was significantly improved using supported catalyst technology, and linear low-density polyethylene (LLDPE) was introduced using this catalyst incorporated with an alpha-olefin comonomer. In 1992 was introduced the latest significant new technology, the single-site catalyzed or metallocene-catalyzed polyethylene resins, resulting in the commercial introduction of several new polyethylenes. [1]

According to *Figure 1*, it is possible to observe the main innovations in PE production over time.

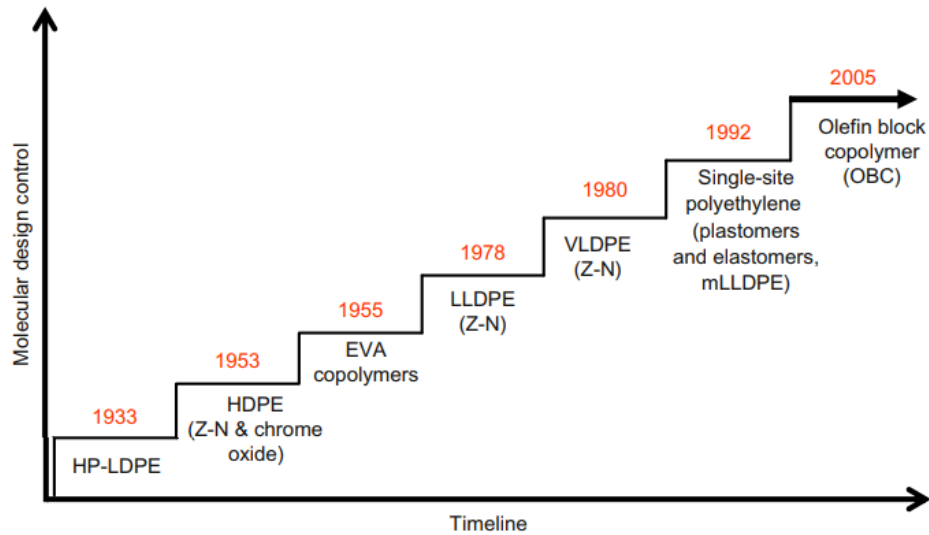


Figure 1- Polyethylene innovations versus time. Adapted from [3]

As stated earlier, the polymerization of ethylene produces PE. In turn, ethylene can be obtained in several ways [4], Figure 2.

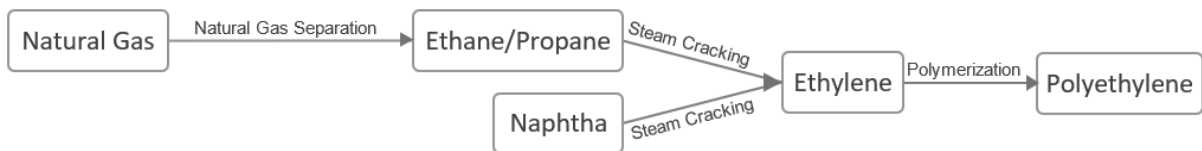


Figure 2- Ethylene Production Technologies

Nowadays, it is being considered routes to new trends in the production of PE, as is the case of obtaining ethylene by the process of methanol to olefins and dehydration of ethanol.

As can be seen in Figure 2, from steam cracking is generally obtained ethylene, so it is common to find in a petrochemical complex, a refinery, a cracker and a polymer plant, located on a single site. This situation represents the high capital investment required for PE production, even though that the final consumer product is very cheap and disposable. Therefore, PE production techniques improvement and development have been the subject of several studies with the essential objective of reducing manufacturing cost. [5]

As regards the polymerization of ethylene, under the right conditions, after the double bond of the ethylene monomer opens up, many monomers link up, which results in the formation of long chains.

As mentioned earlier, two ways can be followed to obtain PE. The first way consists of the high pressure polymerization that produces LDPE, in an autoclave or tubular reactor. The second way consists of the low pressure catalytic polymerization producing LLDPE and HDPE.

The second way can be used three types of catalyst, Ziegler/Natta, Cr/Mo oxide, and Metallocene, in three different processes, solution, slurry, and gas phase processes. The last two processes are the most used.

This work focuses only on the production of PE in gas-phase. According to this process, the polymerization reaction takes place in a fluidized bed reactor (FBR). PE production process widely uses FBR due to its several advantages such as high heat and mass transfer rates, simple construction, considerable particles mixing rate, and capability of continuous transport. [6] In this reactor, small catalyst particles are continuously fed into the reactor that reacts with the incoming gaseous monomer to produce polymer particles with a broad size distribution that directly affect the quality of the final product, mixing/segregation, and hydrodynamic parameters.

Ethylene polymerization is a highly exothermic reaction, and the produced heat must be removed as soon as possible to keep the temperature constant in the reactor. Otherwise, it may lead to hot spots or lump formation. The injection of a cooled gas stream and inert monomer removes the exothermic heat. [3]

Regarding the chemical reaction efficiencies, transfer properties, and energy consumptions always depend on the reactor temperature field and the solid mixing/contacting state, which relies on the particle flow patterns in FBRs.

Thus, an efficient reacting gas and solid particle flow and mixing are of prime importance for FBR operation since that an improper fluidization can lead to an ineffective reaction, heat/mass transfer, inability to maintain uniform distribution of temperature, and accumulation of large polymer particles. The large polymer particles can result in stopping the gasification process due to the choking of the gasifier bed.

To operate FBR more effectively, improve design and scale-up of polydispersed gas phase fluidized bed process is crucial to obtain a fundamental understanding of the gas-solid two-phase flow behaviors considering the temperature fields in the FBR, and a precise prediction of the particles size distribution (PSD) [7] [8].

In this respect, advanced computational methods and computer programming have made it possible for computational fluid dynamics (CFD) to become an efficient technique to predict the macroscopic fluid dynamics, transport phenomena in a gas-solid fluidized bed, and understand the influence of the fluid dynamics on the performance of chemical reactors.

Lately, the CFD models have been employed to analyze the scale-up performance and are an important engineering tool for FBRs at industrial scale predicting their flows.

However, the industrial-scale implies different reactor scales that require different operating conditions and lead to numerous levels of interaction complexity between gas and solid phase, which control the efficiency of the polymerization reaction and product quality. These situations cause some limitations on the application of CFD on an industrial scale. [8] [9][10].

On the other hand, the polymerization kinetics, particle growth, aggregation, and breakage of particles influence the PSD, the population balance model (PBM) should be coupled with the CFD model since PBM is used to compute the size distribution of the dispersed phase. [11] [6].

Several articles have been dedicated to FBR for PE production and its modeling.

Regarding pilot-scale fluidization units, the last articles studied the effect of the method of moments with a 2D CFD-PBM model considering particle growth and aggregation [12], and the temperature field and particle flow patterns with a 3D CFD-PBM model [10] by Yao et al. and Che et al., respectively.

On the other hand, for industrial-scale reactors, Akbari et al. developed a 2D CFD-PBM model for hydrodynamic and particle growth simulation [6], and hydrodynamics and mixing/segregation simulation [9].

This dissertation aims to develop a 3D CFD-PBM model for hydrodynamic and particle growth simulation to an industrial-scale FBR for PE production.

Thus, the main objectives are to 1) develop a CFD model to predict the cold-flow behavior of PE particles in a pilot-scale fluidization unit, 2) perform the CFD model and validate it with experimental data and empirical equations, and 3) develop and perform a CFD model coupled with PBM in an industrial-scale FBR.

Firstly, essential concepts and definitions about PE production and computational models are shown in chapter 2.

Chapter 3 describes the numerical methods to develop the CFD model and CFD-PBM model, simulated in a pilot-scale fluidization unit and an industrial-scale FBR, respectively.

Chapter 4 describe the experimental method to validate the CFD model.

Chapter 5 shows the results of the 3D CFD-PBM developed model.

Finally, chapter 6 summarises these work conclusions, referring to what was achieved and discussing possible future work.

2. OVERVIEW OF POLYETHYLENE PRODUCTION

2.1 Polyethylene

Under the right conditions of temperature, pressure, and catalysis, the double bond of ethylene monomer opens up and many monomers link up to form, in PE elementary form, long backbone chains with an even number of carbon atoms (covalently linked) and two hydrogen atoms attached to each carbon, ending in methyl groups. [13]

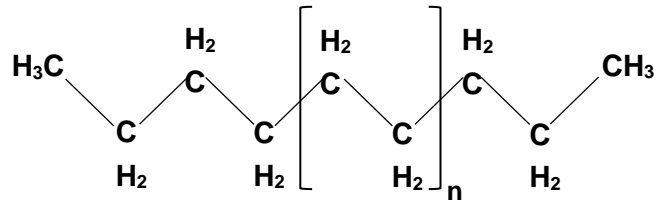


Figure 3 - Chemical structure of pure polyethylene. Adapted from [13]

Chemically pure PE has the chemical formula $C_{2n}H_{4n+2}$, where n is the number of ethylene monomers polymerized to form the chain, also known as the degree of polymerization.

Given that PE can have different degrees of polymerization, up to 250 000, PE consists of molecules of different sizes, sometimes with different compositions, and its molecular weight varies from 1400 to more than 3500000 grams per mole. In the PE molecules can also observe some degree of branching and unsaturation. [13]

That said, melt flow index (MI), and density typically characterizes the many types of PE that exist.

The density of PE depends on the degree of crystallinity, and it increases with increasing degree of crystallinity. In turn, crystallinity is associated with branching and other defects in the chain. Chains that have many defects have a lower degree of crystallinity than those that have few.

About MI, since that it is related to the molecular weight and processability of the product, a polymer with a higher MI will typically have a lower molecular weight and processes easier than a polymer with lower MI. [3]

PE resins can divide into three main classes:

1. High Density Polyethylene (HDPE)

HDPE is the PE type with the highest crystallinity and density due to the extremely low level of branching and its linear structure, Table 1

HDPE can be obtained by slurry, solution, or gas-phase processes that operate at relatively low pressures in the presence of a catalyst and is mixed hydrogen with ethene to control the chain length of the polymer [14] [15]. It is available in a variety of grades, and each one is

optimized for a specific application. It is commonly used in natural gas and water distribution piping and household containers. [16].

Figure 4 describes the different downstream processes/applications of HDPE [1]. Its properties and examples of use are presented in Table 1 and Table 2, respectively.

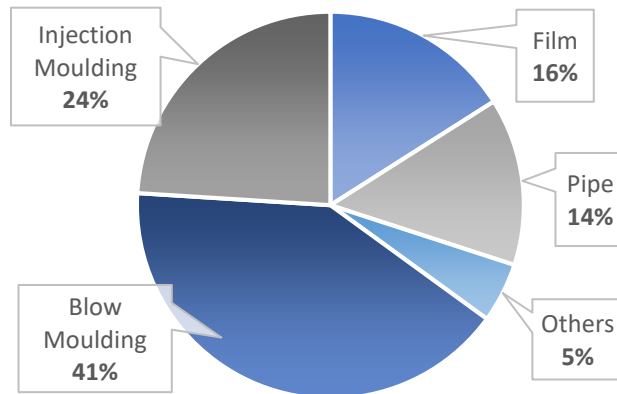


Figure 4- Main downstream processes/applications of HDPE in 2017. Adapted from [14]

2. Low Density Polyethylene (LDPE)

This type of PE is the most easily processed. The high-pressure LDPE process produces both short-chain branches and long-chain branches that hinder the crystallization process, reducing resin density relative to HDPE. LDPE is generally amorphous, transparent, and very flexible material. [15]

Plastic film applications like plastic bags frequently use it due to its properties.

It is produced at high pressure using a tubular or autoclave reactor.

Figure 5 shows the main applications of LDPE. Its properties and examples of use are presented in Table 1 and Table 2, respectively.

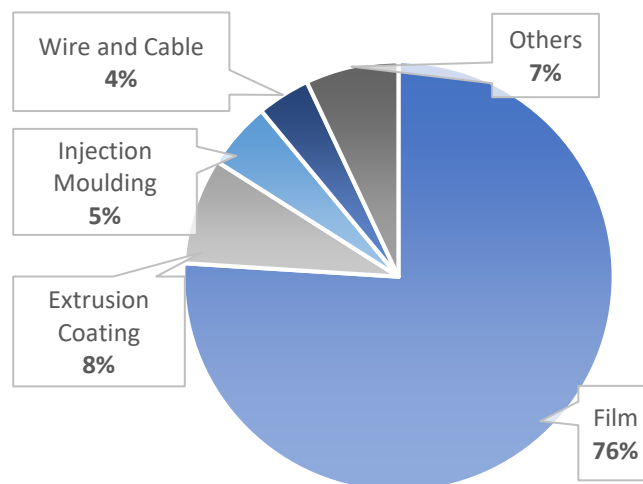


Figure 5- Main downstream processes/applications of LDPE in 2017. Adapted from [14]

3. Linear Low Density Polyethylene (LLDPE)

The copolymerization of ethylene with alpha-olefins using Z-N results in LLDPE production with short chain branches. It is structurally similar to LDPE and competes in the same markets. The main advantage of LLDPE is that the polymerization conditions are less intensive in terms of energy. [16] Density decreases as more enormous amounts of comonomers are incorporated into the copolymer, and these amounts depend upon the target resin.

LLDPE properties and examples of use are presented in Table 1 and Table 2, respectively.

Table 1- Summary of the properties of PE. Adapted from [17] [18]


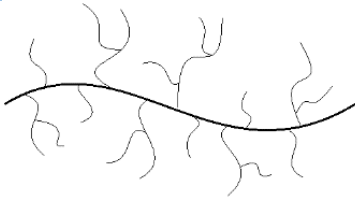
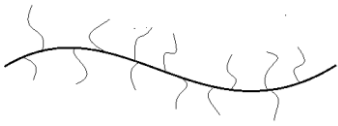
Polymer	HDPE	LDPE	LLDPE
Structure			
Catalyst and Process	Z-N catalyst in: -Single-stage polymerization -Multi-stage polymerization or a Cr or a Philips-type catalyst	Radical polymerization using a tubular reactor or autoclave	Z-N catalyst or a metallocene catalyst
Density (g/cm ³)	0,945 to 0,970	0,915 to 0,940	< 0,930
Crystallinity (%)	60 to 65	45 to 55	30 to 45
Characteristics	-Excellent chemical resistance - High tensile strength -Excellent moisture barrier properties - Hard to semi-flexible	-Flexible and good transparency -Good moisture barrier properties -High impact strength at low temperature -Excellent resistance to acids, bases and vegetable oils	As compared to LDPE, it has: -Higher tensile strength - Higher impact and puncture resistance

Table 2- Examples of uses of PE. Adapted from [18].

Process	HDPE	LDPE	LLDPE
Film	Food packing Shopping bags	Cling film Milk carton lining	Stretch film
Injection molding	Dustbins	Buckets Bowls	Food boxes
Blow molding	Detergent Bottles	Squeezable bottles	-
Extrusion	Water pipes	Flexible water pipes Cable coating	Cable coating

2.2 Polyethylene Production

As explained above, due to the wide range of molecular weight, composition, and branching distributions, PE plays a significant role since it is used for a tremendous variety of products. In order to obtain such characteristics, there are available a variety of catalyst types, several polymerization conditions, and a wide range of processes.

Since PE was first commercialized in the 1960s, there were no significant changes in the process, only a drastic increase in plant production capacity. There was an increase from 80 kton to 750 kton per year for the newest plants. Increased process efficiency and intensification of production allowed an increase in production capacity.

To increase the process efficiency, a thorough knowledge of the reactor is necessary since this is the main element of the process. On the other hand, for full operation of the reactor is still necessary intelligent and deep research on catalysts since it is the coarse topic of the reactor. [19]

Figure 6 shows a general illustration of the basic blocks of an industrial polymerization unit.

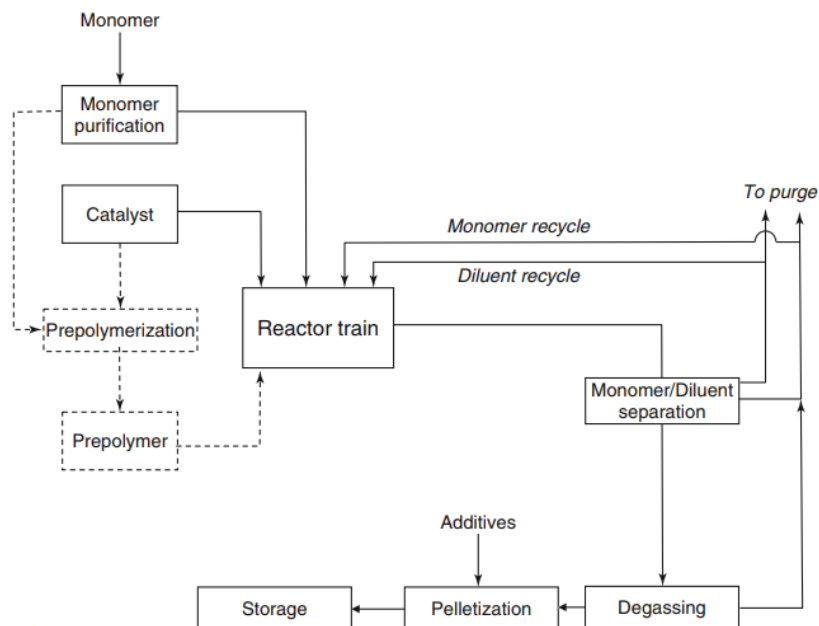


Figure 6 – General schema of polyolefin production unit using Z-N catalysts. [19]

The catalyst, monomer, and other process fluids are fed to the reactor train.

Typically, in slurry conditions, the use of a prepolymerization step is necessary in order to avoid loss of control over the reaction and the morphology due to the high reaction rates during the fragmentation step. Prepolymerization refers to the practice of producing a small amount of polymer on a fresh catalyst particle under mild conditions before injecting it into the main reactor train. This procedure helps to increase the activity of the catalyst in the main reactor and allows

us to produce polymer at a reasonable rate. It means, the particles fragment, but not so much and not too quickly. Heat and mass transfer limitations are reduced to manageable levels or eliminated at all since those particles are grown to a large enough size. [19] Hot spots are more likely to occur in smaller particles, and the reaction is slower since the surface area is smaller.

After exiting the reactor, there is the separation of the diluent, if used, and subsequent recycling of the monomer and diluent to the reactor train. The produced polymer is recovered and subjected to various operations before being stored.

2.2.1 Processes Classification

Two ways can be followed to obtain PE.

The first way consists of the **high pressure** polymerization that produces LDPE with an operating temperature between 80 to 300 °C and operating pressure between 1000 to 3000 bar. The reaction takes place in an autoclave or a tubular reactor and consists of a free-radical-addition polymerization using initiators. The initiator can be either peroxide or oxygen and is injected into the reactor. The major step in this process is the ethylene compression to the reaction pressure through several compression stages with interstage cooling. [1][4]

The second way consists of the **low pressure** catalytic polymerization producing LLDPE and HDPE. The operating pressure range and operating temperature range is between 10 to 80 bar and 70 to 300 °C, respectively.

The second way can be used three types of catalyst, Ziegler/Natta, Cr/Mo oxide and Metallocene, in three different processes [3][4][19]:

- 1. Solution Process** – The reaction takes place mostly in autoclave reactors that operate as CSTRs. Tubular and loop reactors also can be used. Both catalyst and resulting polymer remain dissolved in an inert solvent (hydrocarbon fluid) that must be removed to isolate the polymer. Ethylene, hydrogen, and a comonomer are also dissolved in the inert fluid. The reactor temperature must be kept higher than 150°C to keep the polymer in solution. However, the reaction is highly exothermic, and therefore it is necessary to remove the heat of reaction. The recycled cool solvent and cool fresh ethylene injected into the reactor remove it. After the reaction, the polymer solution is subjected to various operations in order to recover the unreacted monomer, solvent, and isolate the polymer as previously stated. The unreacted monomer and solvent are recycled. Solution processes are most adaptable to the metallocene catalyst system since catalyst does not need to be supported.
- 2. Slurry Process** – The reaction takes place in autoclave or loop reactors that operate with two phases. Both configurations operate as CSTRs. The loop reactors require this configuration due to the high recirculation ratios. The solid phase is the polymer, and the liquid phase contains ethylene monomer and hydrogen that are continuously bubbled through the diluent (organic hydrocarbon fluid). Since ethylene liquefaction is not economically viable, the use of diluent is the alternative that allows the PE production in slurry. The catalyst and polymer formed during the production never dissolve in the diluent fluid. As soon as the polymer forms, it crystallizes, and solid particles are created

in the solvent. The reactor temperature must be kept below the polymer melting point (typically less than 100°C) to keep the polymer in the solid phase. In order to maintain this temperature, the exothermic heat of the polymerization reaction is removed by jacket cooling the loop. The central catalyst systems used in slurry reactors are Ziegler-Natta, Chrome oxide based, and Metallocene. This process requires the purchase, purification, removal, and recycling of the solvent.

- 3. Gas-Phase Process** – The polymerization reaction takes place in a FBR. No solvent is used, the ethylene monomer in the gaseous state is blown into the reactor, and the supported catalyst is continuously fed above the distributor plate. As the PE molecule is polymerized, it precipitates as a solid dispersed, as a fluid bed in the reactor. The gas circulates through the polymerizing fluidized bed, and the reactor temperature must be kept below 115°C to prevent the solid melting. The injection of a cooled gas stream and inert monomer removes the heat of reaction. The main catalysts used are Ziegler-Natta, Chrome oxide based, and Metallocene.

Comparing the different processes, the advantage of using slurry rather than gas phase process is the higher heat transfer capacity due to particles being suspended in a liquid. The indicated means shorter reactor residence times than gas-phase reactors since can be tolerated higher specific reaction rates. On the other and, all steps required to treat the solvent lead to a higher production cost.

As compared to slurry and gas-phases, solution processes operate at a much higher pressure and temperature to ensure that the polymer remains dissolved in the reaction medium. Combining this with the fact that active sites are not supported and, therefore, not subject to mass transfer resistance, means that the polymerization rates in this process are much higher.

However, for the solution process reactors, high viscosities are a limitation, so it is necessary to reduce the polymer concentration in the solution.

Regards the gas-phase process, once that the monomer is in the gas-phase, it is easier to separate the polymer from the unreacted monomer. Since there are no liquids in the reactor, there is no need to flash off large amounts of liquids that represents a significant operating cost reduction since it is a step with high energy demand. It is also possible to obtain an extended product range as there is no solubility limit in the reaction medium.

Although gas species has poor thermal characteristics, some special steps are taken to enhance heat transfer and to keep gas-phase reactors economically competitive in terms of productivity. This step can be an injection of small amounts of liquid components below their dew points or the use of inert gas-phase compounds with higher heat capacities.

Of all processes, the most used is the gas-phase process since it has as main advantages low operating temperature and pressure, no solvent required, better reaction heat removal, low investment capital costs, and flexible production. [20][21][19]

This work focuses only on the gas-phase process with a Z-N catalyst. The following Figure 7 illustrates the process.

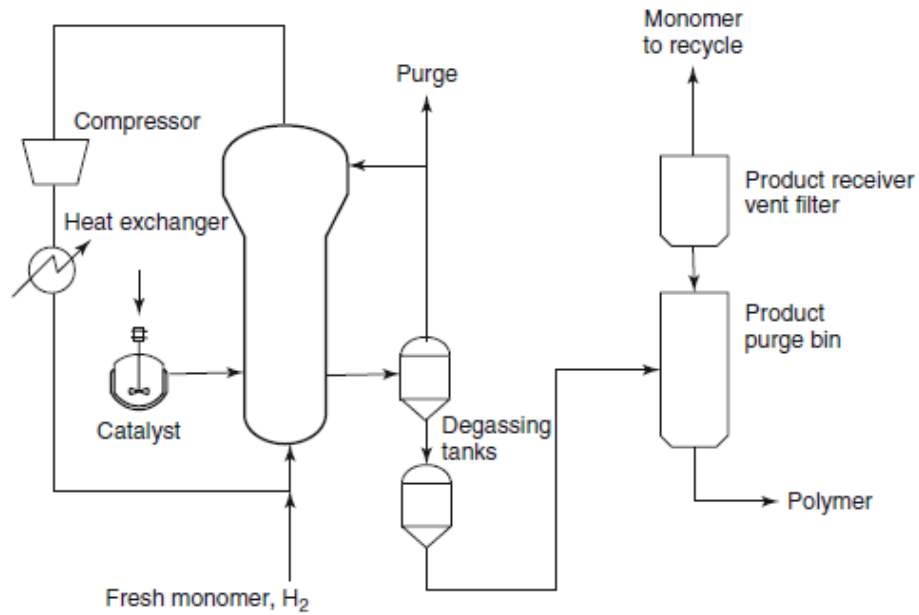


Figure 7- Unipol process for PE manufacture. [19]

2.2.2 Gas-phase reactors

In the industry are used four types of gas-phase reactors: FBR, vertical stirred bed reactor (VSBR), horizontal stirred bed reactor (HSBR), and the multizone circulating reactor (MZCR). However, due to the high enthalpy of polymerization (3600 kJ/kg), FBR is the only type of reactor used to make PE in gas-phase processes because they have the best heat removal capacity of any of the gas-phase reactors. [19]

I. Fluidized Bed Reactor [19][21][22]

The FBR is essentially an empty cylinder with a distributor plate at the bottom and divides into three zones: reaction zone, freeboard zone, and disengagement zone. A schema of an FBR is shown in Figure 8.

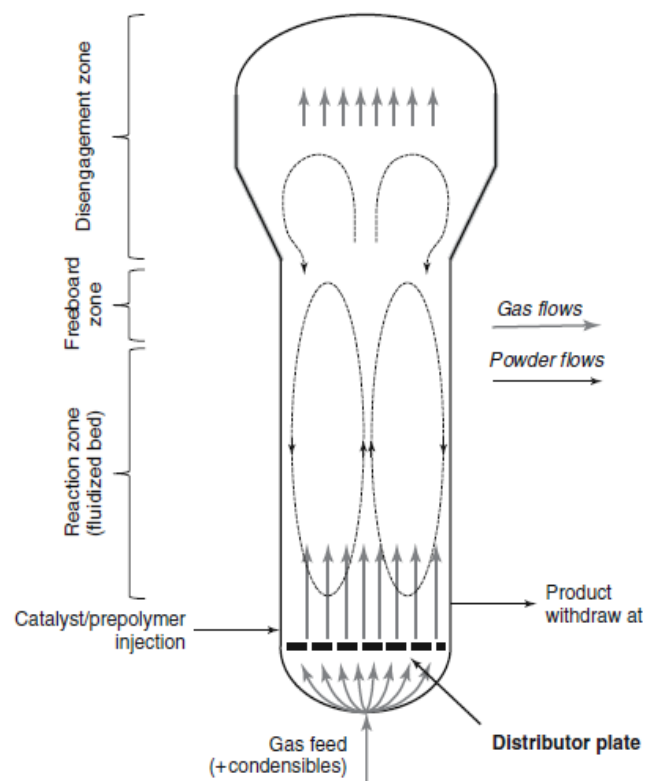


Figure 8- Schematic diagram of an industrial fluidized-bed polyethylene reactor. [19]

The reaction zone, with a height of 10-15 m, locates immediately above the distribution plate and below the freeboard zone. As the name indicates, it is where the polymerization takes place.

As mentioned above, the injection of catalyst is above the distributor plate, and product particles are also withdrawn at similar bed height. The catalyst injection might be done using propane than nitrogen to avoid hot spots in the feed zone because propane has a higher heat capacity.

The central role of the distributor plate is to distribute the components in the powder bed in a proper manner. The injection of fresh feed and recycled gases takes place below the distributor plate. The holes in the plate allow the gases to pass and orient them in order to promote fluidization. The configuration of the holes must prevent particle deposition on the plate and blockage of gas flow. With a reduced gas flow rate into the reactor, the heat removal capacity decreases, resulting in the polymer meltdown inside the reactor. That is, the gas flow rate must be sufficient to ensure the fluidization of the larger particles, so superficial gas velocity is between 0,5-1 m/s, and the relative gas-particle velocity is 2-8 times the minimum fluidization velocity. In order to achieve such high flow rates, typically uses recycle ratios up to 50, with lower per pass conversion, 2-30%. However, conversions are usually higher than 95%.

After the reaction zone, the unreacted gases with fine particles enter into the disengaging zone that facilitates the separation of solids from the gas. As can be seen in Figure 7, the recycled free of solids is recovered at the top of the bed, and then it is compressed and cooled before being fed back to the reactor. Sometimes, the recycled stream can include condensable material to improve heat removal capacity.

It is possible to separate the solids from the gas in the disengagement zone since the width of the disengagement zone at the top of the reactor is at least two times wider than the reactor bed.

The freeboard zone separates the reaction zone and the disengagement zone. At this zone, the void fraction is near one, and generally, particle velocity is below minimum fluidization velocity. It means that some particles will fall back into the bed. The particles small enough get blown through the freeboard zone. To minimize the amount of particles passing through the freeboard zone, the diameter in the disengagement zone is increased so that the superficial gas velocity decreases. The small particles will fall out of the gas phase and back into the main bed of the reactor. However, there is still a fraction of lost particles.

The minimum fluidization velocity must be guaranteed, so there is no collapse of the fluidized bed, but at the same time, a high superficial velocity can pneumatically transport the particles.

On another hand, there are some limitations on the increase of the gas flow rate since the bigger the rate, the smaller the conversion for each pass, and the recycle ratios increase.

Depending on the velocity, different fluidization regimes may occur, as shown in Figure 9.

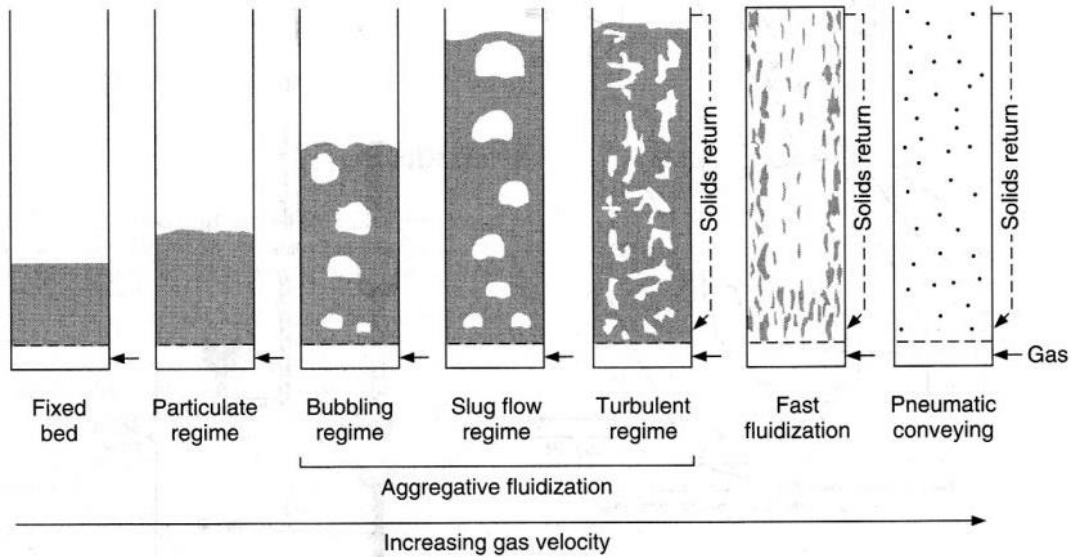


Figure 9-Fluidization regimes [22]

Generally, there is the formation of gas bubbles along the bed, with a small fraction of gas flowing between the particles. The flow behavior depends on the number of bubbles and their size. In turn, it depends on the nature, the type, and the size of the particles, the type of distributor, surface velocity, and bed height.

For gas velocity much higher than the minimum fluidization velocity, the transition from bubbling to turbulent and rapid fluidization occurs. This phenomenon occurs when bed expansion is too high.

For even higher gas velocities, the particles are entrained by the gas and can be recovered by cyclones and thus return to the bottom of the bed. This system is called a recirculating bed. It is practically a pneumatic transport.

The FBRs used in PE production tend to operate in a bubbling regime.

The pressure drop in FBRs is one of the crucial parameters in the proper scale-up and design of FBRs. When the particles in FBRs are fluidized, the pressure gradient can be calculated according to the following classical equations [31],

$$\Delta P_s = (\rho_s - \rho_g)(1 - \epsilon)gL \quad (1)$$

$$\Delta P_g = \rho_g \epsilon gL \quad (2)$$

2.2.3 Kinetic Model ^{[10] [23] [24][25]}

The ethylene polymerization process to produce PE is a type of coordination polymerization which uses Z-N catalysts in the process.

In its broadest definition, Ziegler–Natta catalysts are composed of a transition metal salt of metals from groups IV to VII and a metal alkyl of base metal from groups I to III. The preferred cocatalysts are alkyl aluminum compounds such as trimethylaluminum (TMA), triethyl aluminium (TEA), and diethyl aluminum chloride (DEAC).

Ziegler–Natta catalysts can be heterogeneous or homogeneous, whereas the most common type of heterogeneous Ziegler–Natta catalyst is TiCl₄ supported on MgCl₂ or SiO₂ and is prepared in four main steps: digestion, activation, washing, and drying.

Ethylene polymerization kinetics using Ziegler–Natta catalysts is relatively complicated, and the chemical kinetic scheme comprises a series of elementary reactions, namely, site activation, propagation, site deactivation, chain transformation, and chain transfer reactions, Table 3.

For the reduction of computational cost, the temperature changes only for heat release of chain propagation reaction and heat transfer between two phases, and even though the cooling of the walls occurs in FBRs, only a small amount of heat is removed through them. For this reason, these reactors are often considered adiabatic.

In order to describe the kinetics of ethylene polymerization in CFD modeling, a kinetics model containing the mainly elementary chain propagation reaction is adopted and the polymerization rate R_p can be calculated as

$$R_p = k_p [C][M] \quad (3)$$

where $[M]$ is the concentration of monomer, $[C]$ is the concentration of catalyst active site and k_p is the propagation rate defined as,

$$k_p = k_{p0} \exp\left(-\frac{E_a}{RT}\right) \quad (4)$$

The heat produced from polymerization reaction is expressed as

$$\Delta Q_{rs\alpha} = R_p \Delta H \quad (5)$$

Table 3- Elementary reactions and rate constants of PE polymerization process. Adapted from [26]

Description	Reactions
Formation reaction	$N^*(j) + co - catalyst \xrightarrow{k_f(j)} N(0,j)$
Initiation reaction	$N(0,j) + M \xrightarrow{k_{i_i(j)}} N_i(1,j) \quad i = 1, 2, \dots$
Propagation	$N_i(r,j) + M_k \xrightarrow{k_{p_{ik}(j)}} N_k(r+1,j) + Q(r,j) \quad i = k = 1, 2, \dots$
Transfer to monomer	$N_i(r,j) + M_k \xrightarrow{k_{fm_{ik}(j)}} N_k(1,j) + Q(r,j) \quad i = k = 1, 2, \dots$
Transfer to hydrogen	$N_i(r,j) + H_2 \xrightarrow{k_{fh_i(j)}} N_H(0,j) + Q(r,j) \quad i = 1, 2, \dots$
	$N_H(0,j) + M_i \xrightarrow{k_{hi(j)}} N_i(1,j) \quad i = 1, 2, \dots$
	$N_H(0,j) + AlEt_3 \xrightarrow{k_{hr(j)}} N_1(1,j)$
Transfer to co-catalyst	$N_i(r,j) + AlEt_3 \xrightarrow{k_{fr_i(j)}} N_1(1,j) + Q(r,j) \quad i = 1, 2, \dots$
Spontaneous transfer	$N_i(r,j) \xrightarrow{k_{fs_i(j)}} N_H(0,j) + Q(r,j) \quad i = 1, 2, \dots$
	$N_i(r,j) \xrightarrow{k_{ds(j)}} N_d(j) + Q(r,j) \quad i = 1, 2, \dots$
Deactivation reactions	$N(0,j) \xrightarrow{k_{ds(j)}} N_d(j)$
	$N_H(0,j) \xrightarrow{k_{ds(j)}} N_d(j)$
Reactions with poisons	$N_i(r,j) + I_m \xrightarrow{k_{di(j)}} N_{dIH}(0,j) + Q(r,j) \quad i = 1, 2, \dots$
	$N_H(0,j) + I_m \xrightarrow{k_{di(j)}} N_{dIH}(0,j)$
	$N(0,j) + I_m \xrightarrow{k_{di(j)}} N_{dIH}(0,j)$

2.3 Computational Models

2.3.1 Computational Fluid Dynamics [27]

Computational fluid dynamics (CFD) is a method of predicting fluid flow, heat and mass transfer, chemical reaction, and other related phenomena by numerically solving the equations that characterize these phenomena.

To operate FBR more effectively is crucial to obtain a fundamental understanding of the gas-solid flow behaviors in these reactors. Because of these reasons, computational fluid dynamics (CFD) has become a popular numerical analysis tool to study the gas-solid fluidization systems and to predict flows in FBRs at industrial scale.

As previously stated, the polymerization reaction is hugely exothermic, and if the heat of the reaction is not efficiently removed, it can lead to hot spots in the system. These hot spots can downgrade reactor safety and polymer properties.

Therefore, CFD is becoming a vital engineering tool to predict flow and temperature fields in various types of apparatus of industrial-scale since it is necessary for an ideal mixing and heat transfer.

I. Eulerian-Eulerian Two Fluids [24] [28] [29] [30]

There are generally two categories of CFD modeling for multiphase flow: Eulerian-Eulerian and Eulerian-Lagrangian approaches.

In the Eulerian-Eulerian approach, the gas and solid phases are treated as interpenetrating continua in an Eulerian framework. The continuity and conservation equations are solved for each phase.

On another hand, in the Eulerian-Lagrangian approach, each particle is tracked using a Lagrangian approach, and Navier-Stokes equations are solved for the continuous (Eulerian) phase. This second approach has as a disadvantage the fact that it is limited to a smaller concentration of particles and the computationally demanding when tracks many particles.

The Eulerian-Eulerian approach was used to describe the gas-solid two flows in this work. The gas phase is considered as the primary phase, whereas the solid phase is considered as the secondary or dispersed phase.

The continuity equations of gas and solid phases can be written as

$$\frac{\partial}{\partial t}(\alpha_g \rho_g) + \nabla(\alpha_g \rho_g v_g) = -\dot{m}_{gs} \quad (6) \quad \text{and} \quad \frac{\partial}{\partial t}(\alpha_s \rho_s) + \nabla(\alpha_s \rho_s v_s) = \dot{m}_{gs} \quad (7)$$

where the mass transfer from the gas phase to the solid phase can be calculated as

$$\dot{m}_{gs} = \frac{1}{2} \pi \rho_s G_{m2} \quad (8)$$

The momentum balance equation for the gas phase is expressed as:

$$\frac{\partial}{\partial t}(\alpha_g \rho_g v_g) + \nabla(\alpha_g \rho_g v_g v_g) = -\alpha_g \nabla p + \nabla \cdot \bar{\bar{\tau}}_g + K_{gs}(v_s - v_g) + \alpha_g \rho_g g - \dot{m}_{gs} v_g \quad (9)$$

and the shear stress of gas phase $\bar{\bar{\tau}}_g$ can be calculated as:

$$\bar{\bar{\tau}}_g = \alpha_g \mu_g (\nabla \cdot v_g + \nabla \cdot v_g^T) \quad (10)$$

The momentum balance equation for solid-phase is expressed as:

$$\frac{\partial}{\partial t}(\alpha_s \rho_s v_s) + \nabla(\alpha_s \rho_s v_s v_s) = -\alpha_s \nabla p + \nabla \cdot \bar{\bar{\tau}}_s - \nabla p_s + K_{gs}(v_g - v_s) + \alpha_s \rho_s g - \dot{m}_{gs} v_s \quad (11)$$

and the shear stress of solid phase $\bar{\bar{\tau}}_s$ can be calculated as:

$$\bar{\bar{\tau}}_s = \alpha_s \mu_s (\nabla \cdot v_s + \nabla \cdot v_s^T) + \alpha_s (\lambda_s - \frac{2}{3} \mu_s) \nabla \cdot v_s \cdot \bar{\bar{I}} \quad (12)$$

The energy balance equations for gas and solid phases are described as (13) and (14), respectively.

$$\frac{\partial}{\partial t}(\alpha_g \rho_g h_g) + \nabla(\alpha_g \rho_g v_g h_g) = -\alpha_g \frac{\partial p_g}{\partial t} + \bar{\bar{\tau}}_g : \nabla v_g - \nabla \cdot q_g + \sum_{p=1}^n (Q_{gs} + \dot{m}_{gs} h_{gs} - \dot{m}_{sg} h_{sg}) \quad (13)$$

$$\frac{\partial}{\partial t}(\alpha_s \rho_s h_s) + \nabla(\alpha_s \rho_s v_s h_s) = -\alpha_s \frac{\partial p_s}{\partial t} + \bar{\bar{\tau}}_s : \nabla v_s - \nabla \cdot q_s + \sum_{p=1}^n (Q_{sg} + \dot{m}_{sg} h_{sg} - \dot{m}_{gs} h_{gs}) + \Delta Q_{rsa} \quad (14)$$

where the specific enthalpy of gas phase, h_g , and the specific enthalpy of solid phase, h_s , can be calculated as

$$h_g = \int_{T_{ref}}^T C_{P,g} dT_g \quad (15)$$

$$h_s = \int_{T_{ref}}^T C_{P,s} dT_s \quad (16)$$

The heat flux of the gas phase q_g and the heat flux of the solid phase q_s can be calculated as

$$q_g = -\alpha_g \kappa_g \nabla T_g \quad (17)$$

$$q_s = -\alpha_s \kappa_s \nabla T_s \quad (18)$$

II. Kinetic Theory of Granular Flow [12] [24] [31] [32]

The kinetic theory of granular flow (KTGF) is based on similarities between the flow of gas molecules and granular material. KTGF is used to describe the rheology of the solid phase and some properties such as the solid viscosity, solid pressure, and granular temperature.

The fluid kinetic theory concepts can be introduced to describe the effective stresses in the solid phase due to particle flow collisional contribution when the particle motion is dominated by collision interaction.

The kinetic theory concepts used in this work were derived by Lun et al. [33] as follows

$$p_s = \alpha_s \rho_s \theta_s (1 + 2g_0 \alpha_s (1 + e_s)) \quad (19)$$

$$\lambda_s = \frac{4}{3} \alpha_s^2 \rho_s d_s g_0 (1 + e_s) \sqrt{\frac{\theta_s}{\pi}} \quad (20)$$

where

$$g_0 = \frac{1}{1 - \left(\frac{\alpha_s}{\alpha_s \max}\right)^{1/3}} \quad (21)$$

The granular temperature, θ_s , represents the fluctuation of the particle velocity, and it is proportional to granular energy, the fluctuating energy of the particles' random motion. The granular temperature is different from solid-phase temperature, and it can be calculated as follows

$$\theta_s = \frac{1}{3} \langle v'_s \rangle^2 \quad (22)$$

A balance of the granular energy associated with particle velocity fluctuations is required to supplement the continuity and momentum balance for both phases. Given this, to calculate the granular temperature the transport equation for granular temperature needs to be solved according to Ding and Gidaspow's model [34],

$$\frac{3}{2} \left[\frac{\partial}{\partial t} (\rho_s \alpha_s \theta_s) + \nabla (\rho_s \alpha_s \theta_s v_s) \right] = (-p_s \bar{I} + \bar{\tau}_s) : \nabla v_s - \nabla (k_{\theta_s} \nabla \theta_s) - \gamma_{\theta_s} - \Phi_{g_s} \quad (23)$$

The first term on the right side corresponds to the generation of fluctuating energy due to shear in the particle phase. The second term corresponds to the diffusion of fluctuating energy on gradients in θ_s . γ_{θ_s} corresponds the dissipation due to inelastic particle-particle collisions and Φ_{g_s} corresponds to dissipation or creation of granular energy resulting from the working of the fluctuating force exerted by the gas through the fluctuating velocity of the particles.

The diffusion coefficient for granular energy, k_{g_s} , is given by Syamlal et al. [35] as

$$k_{g_s} = \frac{15 \rho_s d_s \alpha_s \sqrt{\theta_s \pi}}{4(41 - 33\eta)} \left[1 + \frac{12}{5} \eta^2 (4\eta - 3) \alpha_s g_0 + \frac{16}{15\pi} (41 - 33\eta) \eta \alpha_s g_0 \right] \quad (24)$$

with

$$\eta = \frac{1}{2}(1 + e_s) \quad (25)$$

The collision dissipation of energy γ_{θ_s} is given by Lun et al. [33] as

$$\gamma_{\theta_s} = \frac{12(1+e_s^2)}{d_s\sqrt{\pi}} \rho_s \alpha_s^2 \theta_s^{1,5} \quad (26)$$

$$\Phi_{gs} = -3K_{gs}\theta_s \quad (27)$$

In the transport equation for the granular temperature, the convection and diffusion can be neglected assuming that the granular energy is at steady-state and dissipated locally. Thereby, the simplified transport equation for the granular temperature is as follow

$$0 = (-p_s \bar{I} + \bar{\tau}_s) : \nabla v_s - \gamma_{\theta_s} - 3K_{gs}\theta_s \quad (28)$$

The solid shear viscosity μ_s can be calculated as

$$\mu_s = \mu_{s,col} + \mu_{s,kin} + \mu_{s,fr} \quad (29)$$

$$\mu_{s,col} = \frac{4}{5} \alpha_s \rho_s d_s g_0 (1 + e_s) \sqrt{\frac{\theta_s}{\pi}} \quad (30)$$

$$\mu_{s,kin} = \frac{10\rho_s d_s \sqrt{\theta_s \pi}}{96\alpha_s (1+e_s) g_0} \left[1 + \frac{4}{5} (1 + e_s) \alpha_s g_0 \right]^2 \quad (31)$$

$$\mu_{s,fr} = \frac{p_s \sin \theta}{2\sqrt{I_{2D}}} \quad (32)$$

III. Turbulence Model [27] [28] [36]

A turbulence model is a computational procedure that allows to close the system of mean flow equations and the calculation of the mean flow without first calculating the full time-dependent flow field. It must be simple, accurate, and economical to run.

The classic models are based on Reynolds Averaged Navier-Stokes (RANS) equations. These models can contain zero, one, two, or seven equations, and the calculations are time dependent.

Comparing all RANS model options, the standard $\kappa - \varepsilon$ model was employed in this work since it is robust, economical, long accumulated performance data, and reasonably accurate.

The transport equations for the turbulence kinetic energy κ and the turbulence dissipation rate ε can be written as

$$\frac{\partial}{\partial t} (\rho_m \kappa) + \nabla \cdot (\rho_m \kappa \vec{v}_m) = \nabla \cdot \left(\mu + \frac{\mu_{t,m}}{\sigma_\kappa} \nabla \kappa \right) + G_{\kappa,m} - \rho_m \varepsilon \quad (33)$$

$$\frac{\partial}{\partial t} (\rho_m \varepsilon) + \nabla \cdot (\rho_m \varepsilon \vec{v}_m) = \nabla \cdot \left(\mu + \frac{\mu_{t,m}}{\sigma_\varepsilon} \nabla \varepsilon \right) + \frac{\varepsilon}{\kappa} (C_{1\varepsilon} G_{\kappa,m} - C_{2\varepsilon} \rho_m \varepsilon) \quad (34)$$

where

$$\rho_m = \alpha_s \rho_s + \alpha_g \rho_g \quad (35)$$

$$\vec{V}_m = \frac{\alpha_s \rho_s \vec{v}_m + \alpha_g \rho_g \vec{v}_m}{\alpha_s \rho_s + \alpha_g \rho_g} \quad (36)$$

$$\mu_{t,m} = \rho_m C_\mu \frac{\kappa^2}{\varepsilon} \quad (37)$$

$$G_{\kappa,m} = \mu_{t,m} \left((\nabla \vec{V}_m) + (\nabla \vec{V}_m)^T \right) : \nabla \vec{V}_m \quad (38)$$

with. $C_{1\varepsilon} = 1,44$, $C_{2\varepsilon} = 1,92$ and $C_\mu = 0,09$ as the turbulent model coefficients.

IV. Drag Force Model [24] [28] [29] [37]

In the Eulerian-Eulerian model, the transfer of forces between the gas and particle phases is done by the drag force. In FBRs, the drag model plays an important role in gas-solid two-phase flow modeling, and it can be broadly classified into two categories, the conventional drag models and the structure-based drag models. [30] The first one is derived using the terminal velocity data for a single particle and pressure drop data from a densely packed bed. Seeing that the gas-solid flows in FBRs are naturally unstable with fluctuations, which results from gas-solid interactions, some structure-based drag models linking to the fluctuations were introduced.

The drag force model has a critical effect on the hydrodynamics of FBRs, and several models are used to calculate the drag coefficient, namely the Gidaspow model, the Syamlal-O'Brien model, and Wen-Yu model. In this work, the Wen-Yu model is not used since it is for systems with a solid volume fraction of less than 20% [7]. On the other hand, the main advantage of the Gidaspow drag model is to consider the high value of solid volume fraction as well as low values of the volume fraction. [38]

In this work, the Gidaspow model describes the momentum transfer between the gas and solid phase. [39]

Gidaspow model combines Wen and Yu model (1966) for gas volume fraction larger than 0,8 and the Ergun equation (1952) for gas volume fraction lower than 0,8, covering the whole range of void fraction,

$$K_{sg} = \frac{3}{4} C_D \frac{\alpha_s \alpha_g \rho_g |v_s - v_g|}{d_s} \alpha_g^{-2,65}, \quad \alpha_g > 0,8 \quad (39)$$

$$K_{sg} = 150 \frac{\alpha_s (1 - \alpha_g) \mu_g}{\alpha_g d_s^2} + \frac{7}{4} \frac{\alpha_s \rho_g |v_s - v_g|}{d_s}, \quad \alpha_g \leq 0,8 \quad (40)$$

where

$$C_D = \frac{24}{\alpha_g Re_s} \left[1 + \left(\frac{3}{20} \alpha_g Re_s \right)^{0,687} \right], \quad Re_s \leq 1000 \quad (41)$$

$$C_D = 0,44, \quad Re_s > 1000 \quad (42)$$

The Reynolds number Re_s can be calculated as

$$Re_s = \frac{\rho_g d_s |v_s - v_g|}{\mu_g} \quad (43)$$

V. Heat Transfer Coefficient [29] [30] [37]

The rate of energy transfer between gas and solid phases are expressed as follows:

$$Q_{gs} = h_{gs}(T_s - T_g) \quad (44)$$

$$h_{gs} = \frac{6\kappa_g \alpha_g \alpha_s Nu_s}{d_s^2} \quad (45)$$

For the solid particles placed in a continuously moving gas phase, the Ranz–Marshall correlation for the dimensionless heat transfer coefficients is applied in this work to determine the Nusselt number as follow,

$$Nu_s = 2,0 + 0,6Re_s^{1/2} Pr^{1/3} \quad (46)$$

$$Pr = \frac{C_{p,g} \mu_g}{k_g} \quad (47)$$

2.3.2 Population Balance Model [6][9][24][29][30][37][40]

The real heterogeneous polymerization systems in FBR are polydisperse.

In a fluidized-bed olefin polymerization reactor, small catalyst particles are continuously fed into the bed and react with the incoming gaseous monomer to produce polydisperse polyolefins particles.

In the first stage of the polymerization, the catalyst breaks down into many smaller particles, which are quickly encapsulated by the growing semi-crystalline polymer. During their residence in the reactor, the size of the catalyst particles grows due to polymerization. The aggregation of particles that occurs inside the reactor also contributes to the growth of particles. However, the particle size might decrease due to the particle attrition or breakage. Because of the distribution in polymer particle sizes, the fully grown polymer particles migrate to the bottom where they are removed from the reactor. Meanwhile, fresh catalyst particles and the small particles tend to migrate to the upper space of the reactor and continue to react with monomer. Some might leave the reaction zone with the fluidizing gas.

The reaction system is considered as a gas-solid two-phase system, and the solid phase can be characterized by particle-size distribution (PSD) that is directly related to particle growth, aggregation, and breakage dynamics, as shown in Figure 10.

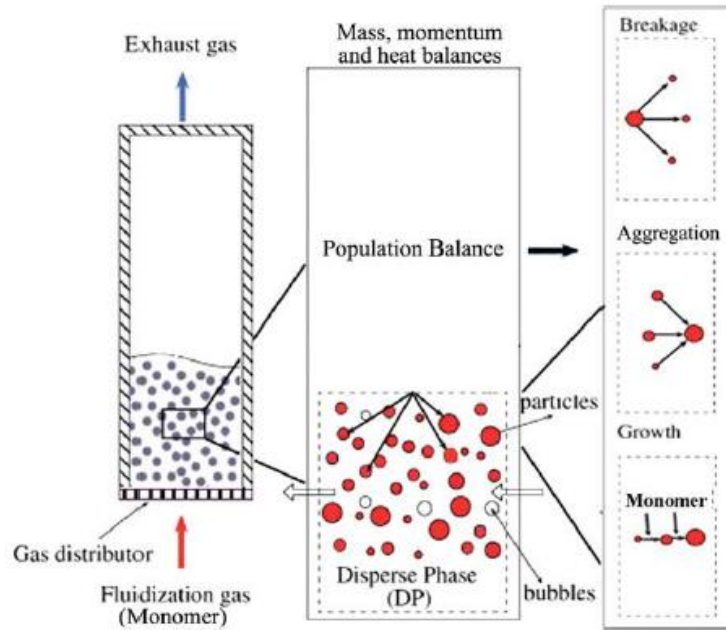


Figure 10- The evolution of particle-size distribution in the fluidized-bed olefin polymerization reactor. [37][24]

When the temperature in the reactor is too low, the particles can break into smaller particles, and when the temperature is too high, approaching the melting temperature of the polymer, the particles can agglomerate to bigger ones. However, to maintain a high production rate, the reactor operating temperature needs to be relatively high. Given this, the particles are mostly affected by aggregation.

The polydispersity can enlarge considering all these aspects.

This PSD also can directly affect the quality of the product, mixing, and hydrodynamic parameters. Thus, to operate FBR more effectively is necessary to obtain a fundamental understanding and describe the gas-solid two-phase flow behaviors of a polymerization system with solid PSD. The CFD model has to be solved together with the PBM.

PBM is a well-established method in computing the size distribution of the dispersed phase and in accounting for the breakage and aggregation effects in multiphase.

A general form of PBM based on the length number density function (NDF) can be expressed as

$$\frac{\partial n(L; \vec{x}, t)}{\partial t} + \nabla \cdot [\vec{u}n(L; \vec{x}, t)] = S(L; \vec{x}, t) = -\frac{\partial}{\partial L} [G(L)n(L; \vec{x}, t)] + B_{ag}(L; \vec{x}, t) - D_{ag}(L; \vec{x}, t) + B_{br}(L; \vec{x}, t) - D_{br}(L; \vec{x}, t) \quad (48)$$

where $n(L; \vec{x}, t)$ is the NDF with particle size, L , as the internal coordinate, \vec{u} is the particle velocity vector, $S(L; \vec{x}, t)$ is the source term representing the particle growth, aggregation, and breakage. $G(L)n(L; \vec{x}, t)$ is the particle flux for the growth rate, $B_{br}(L; \vec{x}, t)$ and $D_{br}(L; \vec{x}, t)$ are the birth and death rates, respectively, of the particles to breakage, and $B_{ag}(L; \vec{x}, t)$ and $D_{ag}(L; \vec{x}, t)$ are the birth and death rates of particles, respectively, for aggregation.

I. Quadrature Method of Moment

Different methods can solve the population balance equation, namely, the discrete method, the inhomogeneous discrete method, the standard method of moments (SMM), the quadrature method of moments (QMOM), and the Direct Quadrature Method of Moments (DQMOM).

In order to track the evolution of the particle size by solving a system of differential equations in lower order moments, the QMOM is applied in this work.

The QMOM requires a relatively small number of scalar equations to track the moments of the population with small errors and provides an attractive option when aggregation quantities, rather than an exact PSD, are desired.

The moments of the particle size distribution (PSD) are determined as

$$m_{kk}(\vec{x}, t) = \int_0^{\infty} n(L; \vec{x}, t) L^{kk} dL, \quad kk = 0, 1, \dots, 2N - 1 \quad (49)$$

where N is the order of quadrature approximation, kk is the specified number of moments.

m_0, m_1, m_2, m_3 are moments with special meaning and are related to some specific things, respectively, total number, length, area, and volume of solid particles per unit volume of mixture suspension.

The Sauter diameter, L_{32} , is used to calculate the mean particle size and can be written as

$$L_{32} = \frac{m_3}{m_2} \quad (50)$$

Applying the moment transformation into the population balance equation, the transport equation for the kk^{th} moment can be written as

$$\begin{aligned} \frac{\partial m_{kk}}{\partial t} + \nabla \cdot [\vec{u} m_{kk}] = & - \int_0^{\infty} kk L^{kk-1} G(L) n(L; \vec{x}, t) dL \\ & + B_{ag, kk}(L; \vec{x}, t) - D_{ag, kk}(L; \vec{x}, t) + B_{br, kk}(L; \vec{x}, t) - D_{br, kk}(L; \vec{x}, t) \end{aligned} \quad (51)$$

where

$$B_{ag,kk} = \frac{1}{2} \int_0^\infty n(\lambda; \vec{x}, t) \int_0^\infty \beta(\lambda, L) (\lambda^3 + L^3)^{\frac{kk}{3}} n(\lambda; \vec{x}, t) dL d\lambda \quad (52)$$

$$D_{ag,kk} = \int_0^\infty L^{kk} n(L; \vec{x}, t) \int_0^\infty \beta(\lambda, L) n(\lambda; \vec{x}, t) dL d\lambda \quad (53)$$

$$B_{br,kk} = \int_0^\infty L^{kk} \int_0^\infty a(\lambda) b(L|\lambda) n(\lambda; \vec{x}, t) dL d\lambda \quad (54)$$

$$D_{br,kk} = \int_0^\infty L^{kk} a(L) n(L; \vec{x}, t) dL \quad (55)$$

where $\beta(\lambda, L)$ is the aggregation kernel representing the rate coefficient for aggregation of two particles with lengths L and λ . $a(L)$ is the breakage kernel representing the rate coefficient for breakage of a particle of size L . $b(L|\lambda)$ is the fragment distribution function for the breakage of a particle with length L

The QMOM based on the quadrature approximation can be written as

$$m_{kk} = \int_0^\infty n(L; \vec{x}, t) L^{kk} dL \approx \sum_{i=1}^N w_i L_i^{kk}, \quad kk = 0, 1, \dots, 2N - 1 \quad (56)$$

where the weights, w_i , and abscissas, L_i , are computed through the product-difference algorithm from the lower order moments.

Applying the quadrature approximation, the transport equation for the kk^{th} moment can be written as

$$\begin{aligned} \frac{\partial m_{kk}}{\partial t} + \nabla \cdot [\vec{u} m_{kk}] = & kk \sum_{i=1}^N L_i^{kk-1} G(L_i) w_i + \frac{1}{2} \sum_{i=1}^N w_i \sum_{j=1}^N w_j (L_i^3 + L_j^3)^{\frac{kk}{3}} \beta(L_i, L_j) \\ & - \sum_{i=1}^N L_i^{kk} w_i \sum_{j=1}^N w_j \beta(L_i, L_j) + \sum_{i=1}^N w_i \int_0^\infty L^{kk} a(L) b(L|L_i) dL - \sum_{i=1}^N L_i^{kk} w_i a(L_i) \end{aligned} \quad (57)$$

This equation can be solved following the evolution of w_i and L_i .

Considering that in this work the effect of aggregation and breakage was not considered, the details of the aggregation kernel, the breakage kernel, and the fragment distribution function can be found in Che et al. (2015) [29].

II. Particle Growth Rate

The particle growth begins with particle fragmentation. Taking into account that the supported catalysts used in this process are tremendously porous particles that when they are fed into the reactor, the species present in the continuous phase of the reactor begin to diffuse into their pores. Is used MgCl₂-supported Ziegler–Natta catalysts as it was said previously.

Polymer formation on the surface of the catalyst pores begins as soon as the reactant species reach the active sites of the catalyst and react. The polymer particle starts growing by expansion.

As shown in Figure 11, fragmentation occurs when the polymerization creates forces inside the particles since that polymer accumulation in the active sites generates a local buildup of stress at different points on the surface and cause them to fragment and further expand.

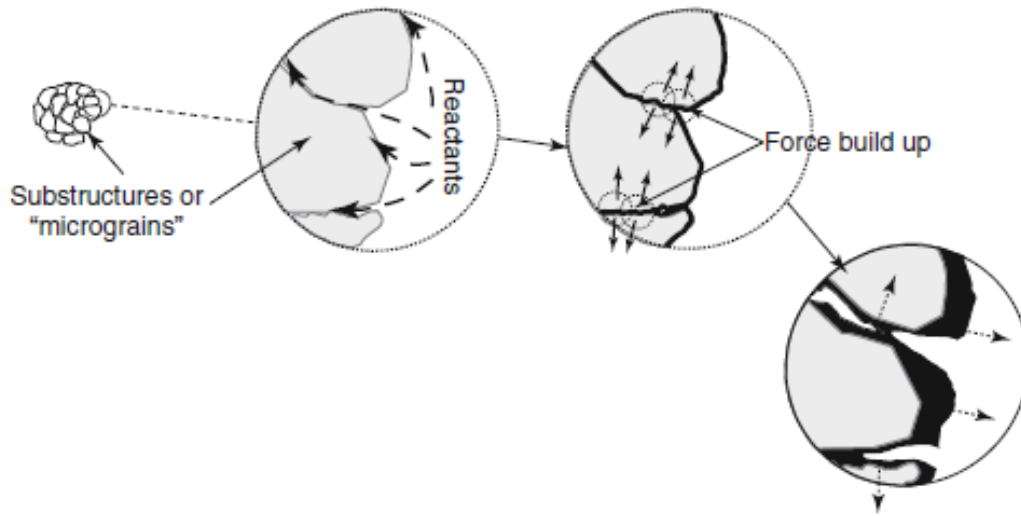


Figure 11- Particle growth evolution. [40]

Therefore, the internal structure of the particles will be a function of the rate of generation of internal mechanical forces and the rate dissipation of energy by the solid.

The local value of PE particle growth rate can be expressed in terms of the overall particle polymerization rate, and it can be calculated as follows,

$$G(L_i) = \frac{d(L_i)}{dt} = \frac{R_p L_0^3}{3\rho_s L_i^2} \quad (58)$$

2.3.3 Coupling between the CFD two-fluid model and PBM

As stated previously, in industrial PE production is necessary to couple the CFD model with PBM. Figure 12 shows the schematic of the coupled approach in the model.

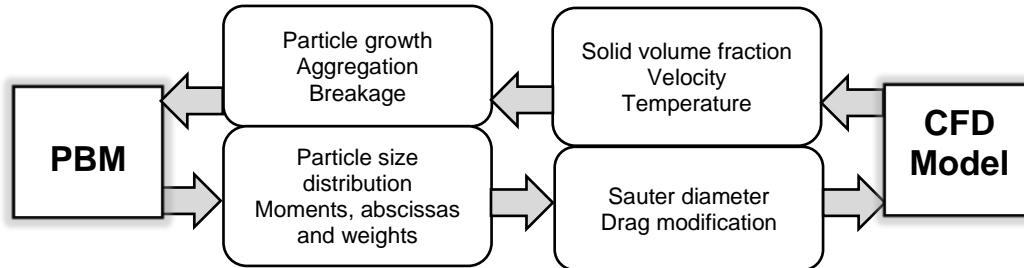


Figure 12-CFD-PBM coupled model. Adapted from [29][37]

The solid volume fraction, particle velocity, and temperature calculated from the transport equations by the CFD model are used to solve PBM because they are related to aggregation, breakage, and particle growth. When PBM is solved, the moments of PSD can be used to calculate the Sauter diameter to modify the interphase force in the two-fluid model further, and then the information of solid volume fraction, particle velocity and temperature for PBM is updated.

Thereby, an integrated coupling between CFD and PBM is achieved. Both CFD and PBM can improve each other in the coupled model.

3. NUMERICAL METHODS

3.1 CFD model- Pilot-scale fluidization unit

In this section, a 3D CFD model is developed to study the cold-flow behavior of PE particles in a pilot-scale fluidization unit. The software ANSYS Fluent 16.0 was used to develop the model.

The population balance, polymerization heat, and polymerization kinetics are not considered. In order to get the right prediction of the particle flow behavior and the bed pressure drop of PE particles were defined the geometry, mesh, and setup simulation data for the pilot-scale fluidization unit.

3.1.1 Geometry

The pilot-scale fluidization unit geometry has been designed according to the equipment instruction manual provided by the manufacturer. However, some dimensions are not indicated in the manual, so it was necessary to confirm the dimensions in the pilot-scale fluidization unit that is available in the laboratory, Figure 13- Pilot-scale fluidization unit available in the Faculty's laboratory. The photos of the laboratory's unit and the manual used are in ***Appendix B – Pilot-scale reactor dimensions***

The shape of the unit is the pilot-scale of an industrial FBR for PE production.

First, half of the reactor was drawn in 2D, and then, the Revolve tool was used around the chosen axis, y . In order to obtain a better mesh, the reactor geometry was divided into five bodies, but they are all interconnected into one part.

The reactor geometry is shown in Figure 14 and Figure 15.



Figure 13- Pilot-scale fluidization unit available in the Faculty's laboratory

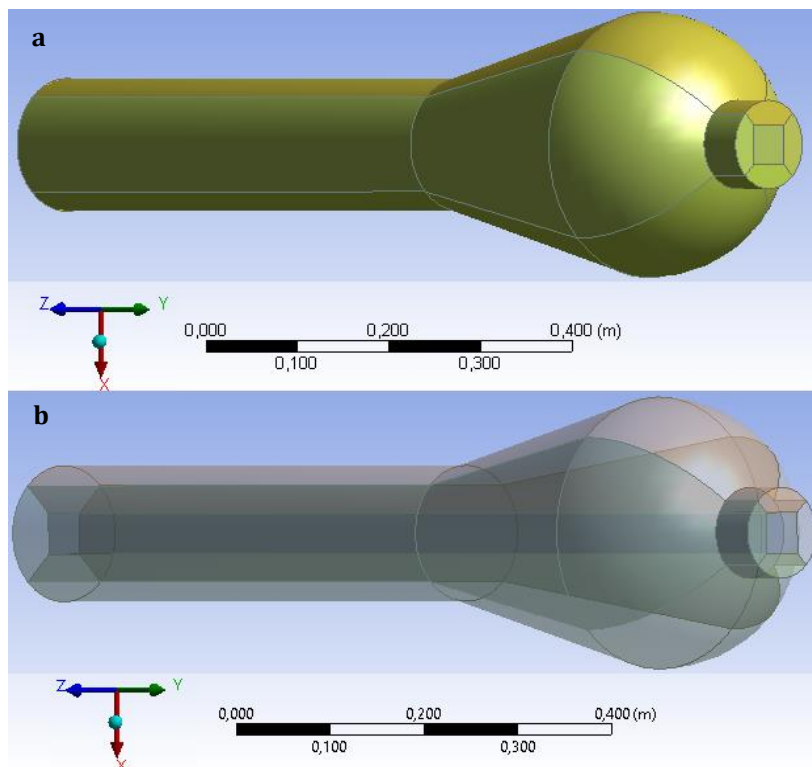


Figure 14-a) pilot-scale fluidization unit geometry b) five bodies of pilot-scale fluidization unit geometry (CFD simulation)

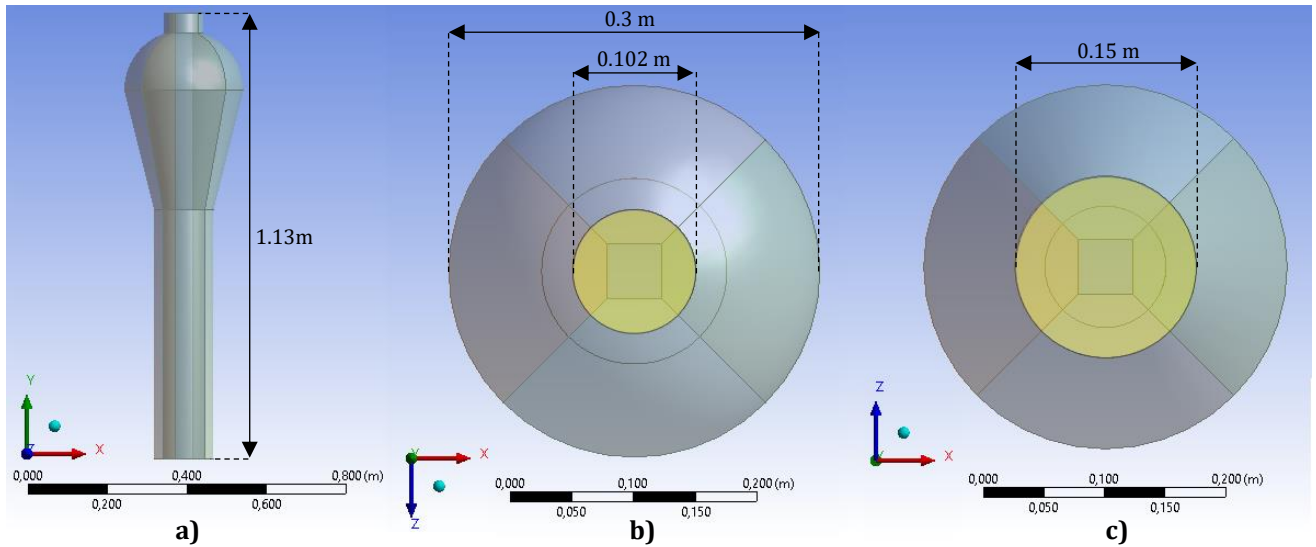


Figure 15- Different perspectives of the pilot-scale fluidization unit geometry a) lateral b) top c) bottom (CFD simulation)

3.1.2 Mesh

In order to get a better mesh quality, I used a multiblock geometry with a structured grid, as shown in Figure 16 and Figure 17. It is more flexible than a single block but still limited.

This structure gives full control of the mesh grading using edge meshing, with high-quality elements [44].

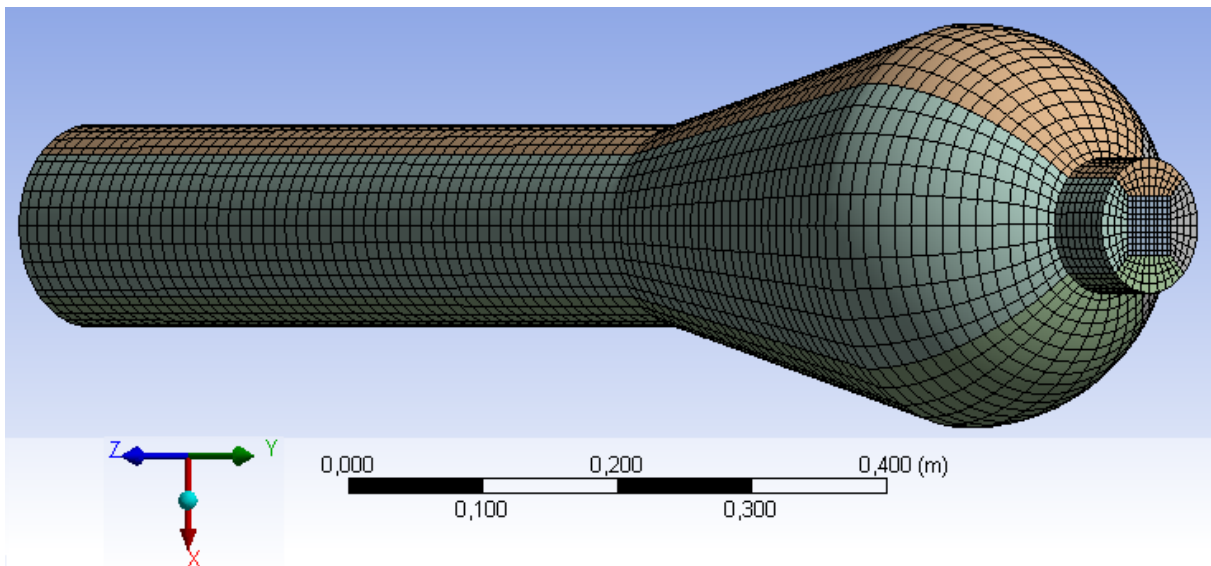


Figure 16- Mesh for the pilot-scale fluidization unit with 118 557 nodes (CFD simulation)

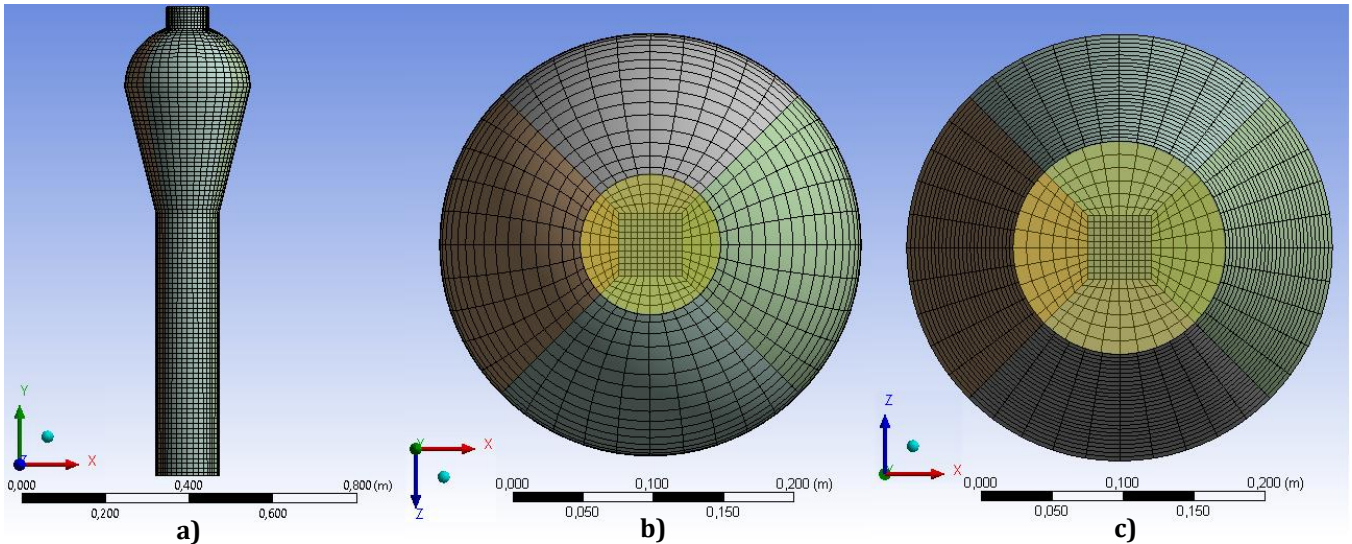


Figure 17- Mesh and boundary conditions for the pilot-scale fluidization unit with 118 557 nodes a) wall b) outlet c) inlet (CFD simulation)

Three different meshes were generated and subjected to sensitivity analysis in order to investigate the adequate number of computational cells to predict the flow behavior. Table 4 shows the number of nodes, skewness, and aspect ratio for each one. These last two are related to the quality of the mesh. Skewness and aspect ratio should be near 0 and 1, respectively. [44][45]

Table 4- Number of nodes and quality parameters for the pilot-scale fluidization unit meshes

Nodes number	Maximum aspect ratio	Skewness
50 152	5,956	0,597
81 624	5,992	0,544
118 557	4,947	0,517

It is possible to verify that the mesh with a higher nodes number, 118 557 nodes, have higher quality by evaluating the parameters presented in Table 4.

According to the sensitivity analysis of the nodes number of the mesh, **C.1. Grid for pilot-scale fluidization unit**, the 118 557 nodes mesh was chosen to perform the simulation.

The average pressure drop for the simulation with 118 557 nodes mesh was 5.91 mbar, with an associated error of 0.34% compared to the theoretical value (5.89 mbar). The theoretical value was obtained from the classical equation (1) and (2).

3.1.3 Setup simulation data

The simulation conditions and the properties of gas and solid phases are displayed in Table 5 and Table 6, respectively.

Table 5- Boundary conditions and model parameters for CFD model simulation in a pilot-scale fluidization unit.

Description	Values
Granular viscosity	Gidspow
Granular bulk viscosity	Lun et al.
Frictional viscosity	Schaeffer
Angle of internal friction	30°
Granular temperature	Algebraic
Drag law	Gidspow
Coefficient of restitution for particle-particle collisions	0.9
Inlet boundary conditions	Velocity inlet
Outlet boundary conditions	Pressure outlet
Wall boundary conditions	No slip for air, specularly coefficient 0 for solid phase
Initial bed height	0.1 m
Initial volume fraction of solid phase	0.63
Operating pressure	1 atm
Inlet gas velocity	3.3 m/s
Turbulent kinetic energy	0.000687 m ² /s ²
Turbulent dissipation rate	0.000128 m ² /s ³
Convergence criteria	0.001
Time step	0.001 s

Table 6- Physical properties of gas and solid phases for CFD model simulation in a pilot-scale fluidization unit

Physical properties	Air	Solids
Density, kg/m ³	1.225	953
Viscosity, kg/(m·s)	1.08·10 ⁻⁵	-
Diameter, μm	-	2500

The gas velocity should be between 2 - 8 times the u_{mf} , as said in **Fluidized Bed Reactor**. Therefore, it was chosen as the most appropriate correlation available in the literature, taking into account the type of polymer particles.

Knowing that the particles belong to group D, calculated in **Appendix A – Particle classification- A.1**, the most appropriate correlation [41] is given by

$$Re_{mf} = (33.95^2 + 0.0465Ar)^{0.5} - 33.95 \quad (59)$$

$$Ar = \frac{g\rho_g(\rho_s - \rho_g)d_p^3}{\mu^2} \quad (60)$$

With $Re_{mf} = 216.45$ and

$$Re_{mf} = \frac{\rho_g d_p u_{mf}}{\mu} \quad (61)$$

the u_{mf} is 0.821 m/s. Thus, the velocity used in the simulation and the experiment with the pilot-scale fluidization unit was $4u_{mf}$, 3.3 m/s. These particles require a much higher velocity to fluidize these solids.

Regarding computational time and convergence, these are usually affected by the time step. Thus, a smaller time step is appropriate for a more precise solution.

For comparing different times steps, the dimensionless Courant number was used. Low Courant number decreases oscillations and numerical dispersion and improves accuracy [42][43]. It was selected a time step that ensured a Courant-Friedrichs-Levy (CFL) number of less than 1.

$$CFL = \frac{v_g \Delta t}{\Delta x} \quad (62)$$

where v_g is the inlet gas velocity, Δt is the time step, and Δx is minimum cell size.

Considering specific conditions in this work, a time step of 0.001 s, $v_g = 3.3$ m/s and $\Delta x = 0.00435m$, the CFL is 0.759, which demonstrates that the time step is indicated for the simulation.

In order to ensure numerical stability and capture mesh independent results, was used small time steps of 0.001 s with 20 iterations per time-step.

3.2 CFD- PBM coupled model- industrial-scale FBR

In this section, the previous 3D CFD model validated in **4.1 CDF model validation- Pilot-scale fluidization unit** is coupled with PBM. This new model is developed to study the flow behavior of PE particles and to track the changes in PSD in an industrial-scale FBR. It is considered the population balance, polymerization heat, and polymerization kinetics.

The software ANSYS Fluent 16.0 was used to develop the model where the geometry and the mesh of the industrial-scale FBR were defined for more ahead predict the particle flow behavior, and the bed pressure drop of PE particles.

3.2.1 Geometry

The industrial-scale FBR geometry has been designed according to two articles that provide the dimensions of an industrial-scale FBR [9][6]. In the articles used to support geometry drawing, not all the dimensions required to draw geometry are defined. The remaining dimensions were defined by similarity ratios between pilot-scale and industrial-scale geometry.

First, half of the reactor was drawn in 2D, and then, the Revolve tool was used around the chosen axis, y .

In order to obtain a better mesh, as we will see next, the reactor geometry was divided into five bodies, but they are all interconnected into one part.

The reactor geometry is shown in Figure 18 and Figure 19.

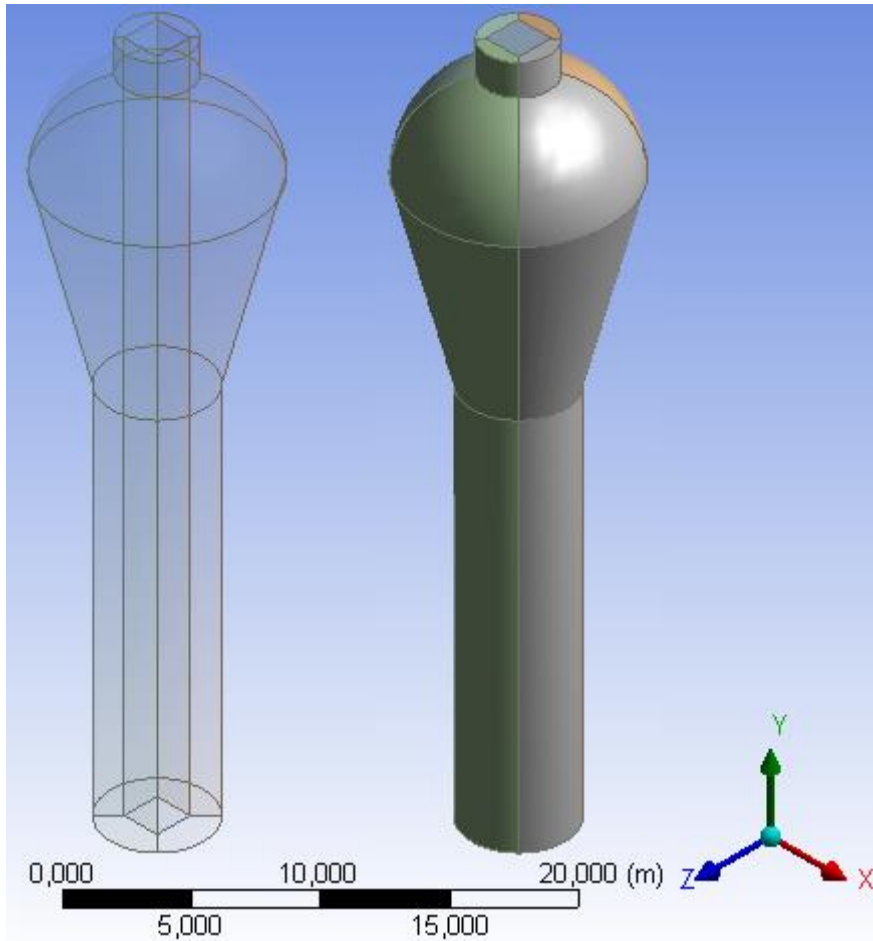


Figure 18-a) industrial-scale FBR geometry b) five bodies of industrial-scale FBR geometry

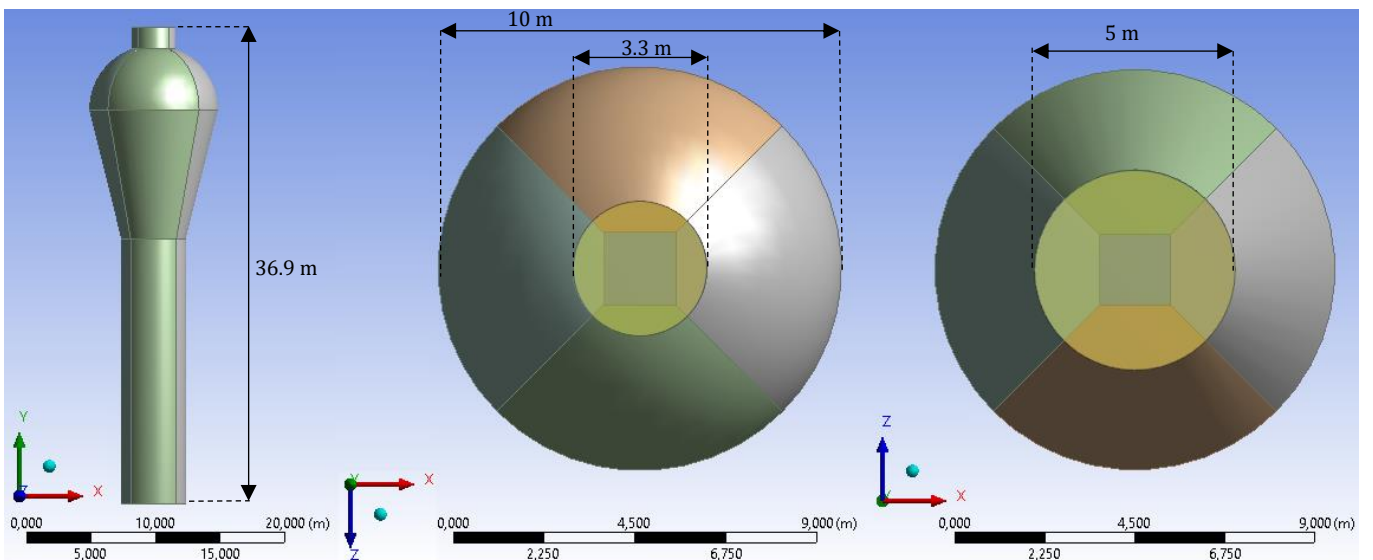


Figure 19-Different perspectives of the industrial-scale FBR geometry a) lateral b) top c) bottom (CFD-PBM simulation)

3.2.2 Mesh

As was done in the previous subchapter, it is essential to get a suitable number of cells that are adequate to predict the hydrodynamics in the FBR and provide grid-independent results.

In order to get a better mesh quality, I also used a multiblock geometry with a structured grid, as shown in Figure 20 and Figure 21. It is more flexible than a single block but still limited. This structure gives full control of the mesh grading using edge meshing, with high-quality elements. [44]

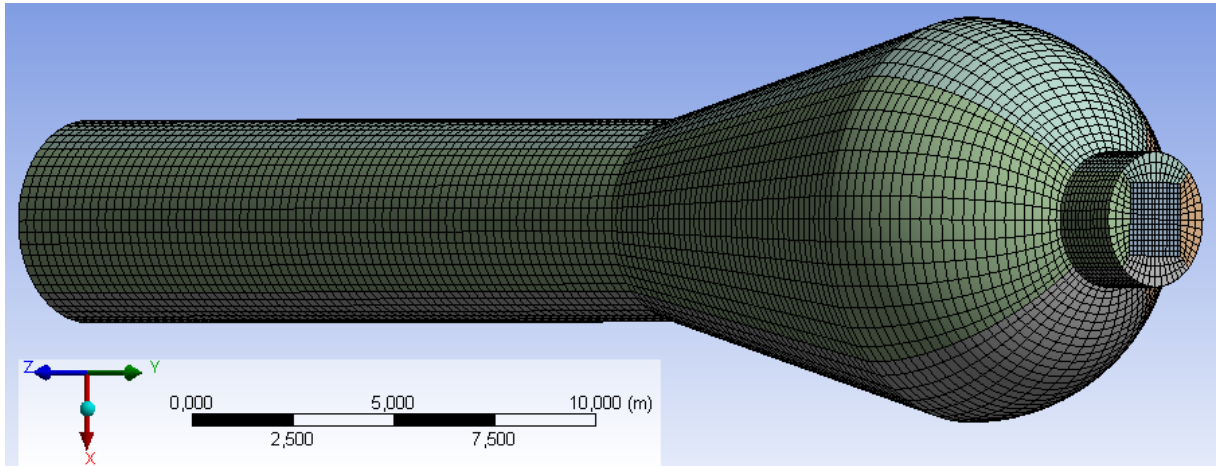


Figure 20- Mesh for the industrial-scale reactor with 309 551 nodes

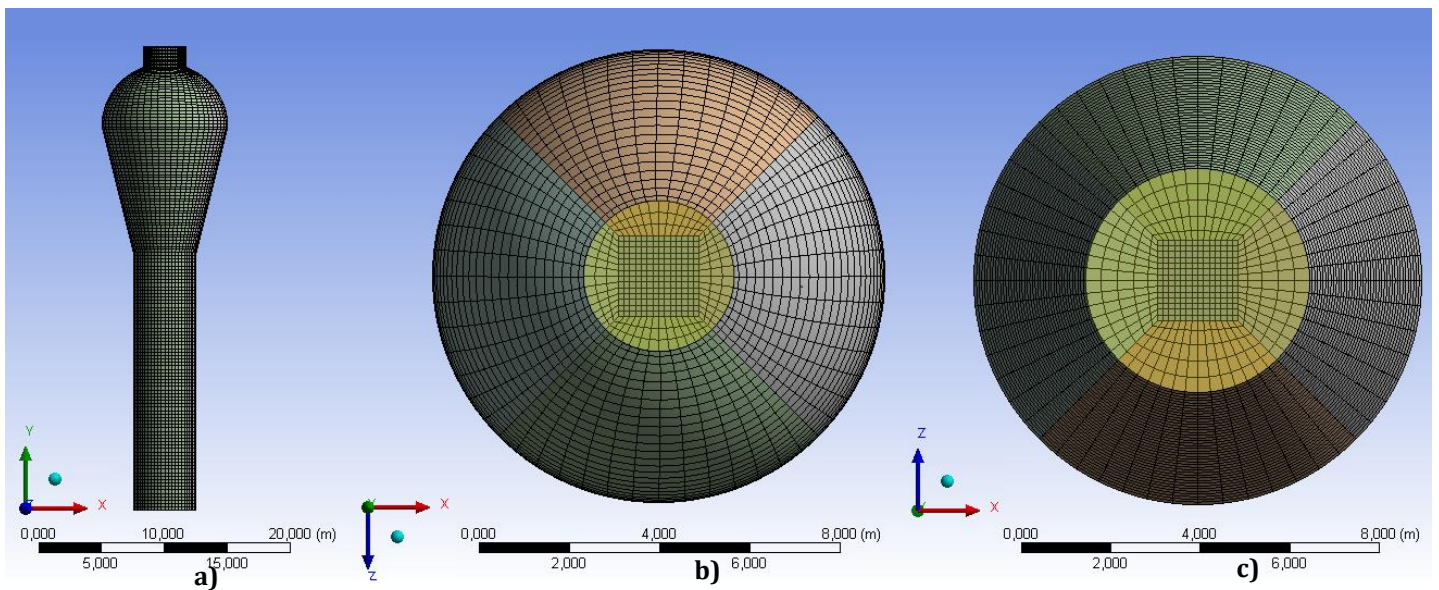


Figure 21-Mesh and boundary conditions for the industrial-scale reactor with 309 551 nodes a) wall b) outlet c) inlet (CFD-PBM simulation)

Three different meshes were generated and subjected to sensitivity analysis in order to investigate the adequate number of computational cells to predict the flow behavior. Table 7 shows the nodes number, skewness, and aspect ratio for each one. As stated earlier, these last

two are related to the quality of the mesh. Skewness and aspect ratio should be near 0 and 1, respectively. [44][45]

Table 7-Number of nodes and quality parameters for the industrial-scale reactor meshes

Nodes number	Maximum aspect ratio	Skewness
157 192	6.711	0.553
249 493	6.450	0.532
309 551	5.451	0.508

It is possible to verify that the mesh with a higher number of nodes, 309 551 nodes, have higher quality by evaluating the parameters presented in Table 7.

According to the sensitivity analysis of the nodes number of the mesh, **C.2. Grid for industrial-scale FBR**, the 309 551 nodes mesh was chosen to perform the simulation.

The average pressure drop for the simulation with 309 551 nodes mesh was 0.4085 bar, with an associated error of 1.65% compared to the theoretical value (0.4153 mbar). The theoretical value was obtained from the classical equation (1) and (2).

3.2.3 Setup simulation data

The particle growth rate equations (described in **2.3.2 Population Balance Model**), polymerization heat, and polymerization kinetics (described in **2.2.3 Kinetic Model**), are all defined using User Defined Functions (UDF), as shown in **Appendix E- User Defined Functions**.

The basic equations for CFD modeling are taken from the previous model used for the pilot-scale fluidization unit. The gas phase properties are not the same since that now, it is considered the real mixture present in the industry and that it is used to produce PE.

The simulation conditions, the properties of gas and solid phases, kinetic variables values, boundary conditions and model parameters are displayed in Table 8, Table 9, and Table 10, respectively.

Table 8- Physical properties of gas and solid phases for CFD-PBM model simulation in an industrial-scale FBR [6][9]

Physical properties	Gas	Solids
Density, kg/m ³	20	850
Viscosity, kg/(m·s)	1.2·10 ⁻⁵	-
Heat capacity, J/(kg·K)	1817	2104
Thermal conductivity (W/(m·K)	0.023065	0.084
Temperature (K)	313	361

Table 9- Kinetic parameters for CFD-PBM model simulation in an industrial-scale FBR [37][29]

Kinetic parameter	Values
E_a , J/mol	33500
ΔH , kJ/mol	100
k_p^0 , $m^3/(mol \cdot s)$	$1 \cdot 10^{-6}$
Heat capacity, J/(kg·K)	2104
Thermal conductivity (W/(m·K))	0.084

Table 10- Boundary conditions and model parameters for CFD-PBM model simulation in an industrial-scale FBR

Description	Values
Granular viscosity	Gidspow
Granular bulk viscosity	Lun et al.
Frictional viscosity	Schaeffer
Angle of internal friction	30°
Granular temperature	Algebraic
Drag law	Gidspow
Coefficient of restitution for particle-particle collisions	0.9
Inlet boundary conditions	Velocity inlet
Outlet boundary conditions	Pressure outlet
Wall boundary conditions	No slip for air, specularity coefficient 0 for solid phase
Initial bed height	10
Initial volume fraction of solid phase	0.498
Operating pressure	2 MPa
Inlet gas velocity	0.38 m/s
Turbulent kinetic energy	0.000687 m^2/s^2
Turbulent dissipation rate	0.000128 m^2/s^3
Convergence criteria	0.01
Time step	0.01 s

The initial particle size distribution used is shown in Figure 22.

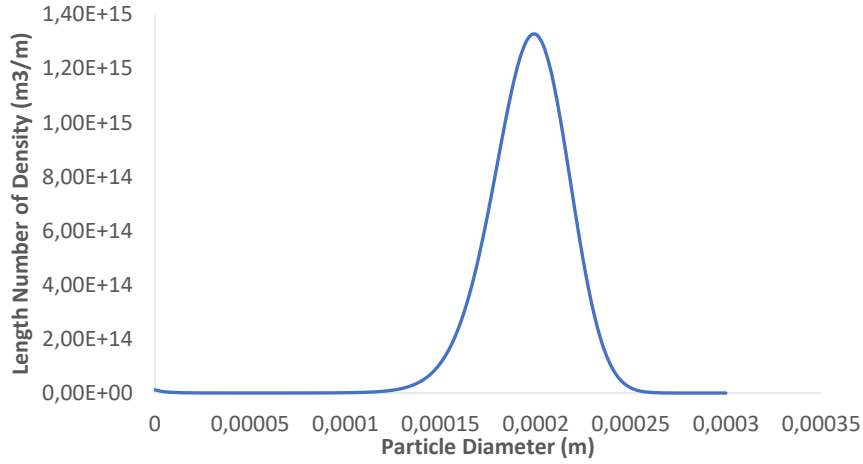


Figure 22- Initial particle size distribution in the industrial-scale FBR for the CFD-PBM simulation. [30]

The velocity used for the simulation is $3 u_{mf}$. The diameter used for the calculations corresponds to the average product size of 0.0012 m. Therefore, the velocity used is three times the minimum fluidization velocity of large particles.

It was necessary to choose the most appropriate correlation available in the literature, considering the type of polymer particles.

Knowing that the particles belong to group B, calculated in **Appendix A – Particle classification-A.2**, the most appropriate correlation [41] is given by

$$Re_{mf} = (27.2^2 + 0.0408Ar)^{0,5} - 27.2 \quad (63)$$

$$Ar = \frac{g\rho_g(\rho_s - \rho_g)d_p^3}{\mu^2} \quad (64)$$

With $Re_{mf} = 256.47$ and

$$Re_{mf} = \frac{\rho_g d_p u_{mf}}{\mu} \quad (65)$$

the u_{mf} is 0.128 m/s. Thus, the velocity used in the simulation was $3 u_{mf}$, 0.38 m/s.

As previously done in the subchapter before, it is necessary to set the time step using the dimensionless Courant number.

Using the equation (62) and considering specific conditions in this work, a time step of 0.01 s, $v_g = 0.38$ m/s and $\Delta x = 0.12355$ m, the CFL is 0.03114, which demonstrates that the time step is indicated for the simulation.

In order to ensure numerical stability and capture mesh independent results, was used small time steps of 0.01 s with 20 iterations per time-step.

4. EXPERIMENTAL METHODS

4.1 CDF model validation- Pilot-scale fluidization unit

After confirming that the simulation values of pressure drop agree with the empirical equation value calculated from equation (1) and (2), **C.1. Grid for pilot-scale fluidization unit**, it is necessary to compare the particle flow behavior verified in the simulation with the experimental one, observed for the same velocity.

The simulation was performed for two different velocities, 3.3 m/s (Re=870), and 5.7 m/s (Re=1520). However, in the laboratory, particle flow behavior was recorded at three different velocities, 0.9 m/s, 3.3 m/s and 5.7 m/s.

As was said previously, when the solid particles are fluidized at different velocities, the bed behaviors are obtained in different regimes, Figure 9. Thus, it is essential to know what type of regime occurs for the velocities used.

At minimum fluidization, the bed behaves as a pseudo-liquid. For Group D, a further increase in gas flow can cause the extra gas to flow in the form of bubbles, so the u_{mf} is equal to minimum bubbling velocity, u_{mb} .

On the other hand, the bubble size increases when the fluidizing velocity of the bed height is increased, and the bed is small in cross-section. The bubble may increase to a size comparable to the diameter of the bed, passing through the bed as a slug – *slugging*. This is not usual in commercial FBR since the diameter is large enough. The minimum slugging velocity, u_{sl} , is given as [46],

$$u_{sl} = u_{mf} + 0,07(gD)^{0,5} \quad (66)$$

Considering the bed diameter, D , and the u_{mf} calculated previously, $u_{sl} = 0.91 \text{ m/s}$.

In the bubbling regime, the bed expands, and a continued increase in the velocity may eventually show a change in the pattern of the bed expansion. The bubble fraction increases until it reaches a stage when the bubble phase changes due to fast coalescence and breakup. This results in a violently active and highly expanded bed referred to as a *turbulent bed*. The transition from bubbling to a turbulent bed does not take place abruptly. The pressure drop across the bed fluctuates randomly with a peak at the velocity u_c , and then reduces to a steady value as the fluidizing velocity is increased further to the velocity u_k , as shown in Figure 23.

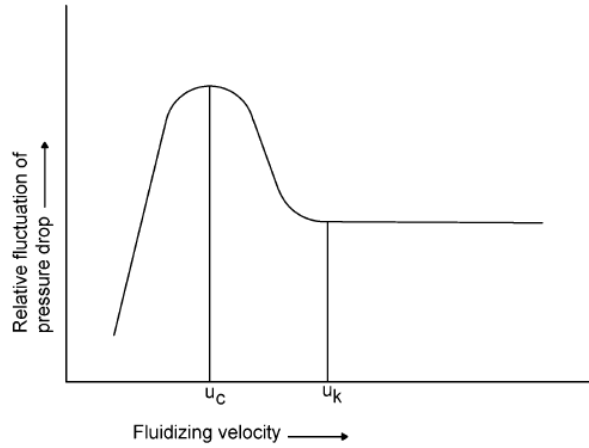


Figure 23- Amplitude of pressure fluctuation across the bed increases as the bed approaches turbulent fluidization.

The transition velocities can be calculated as [46],

$$Re_c = \frac{u_c d_p \rho_g}{\mu} = 0,936 Ar^{0,472} \quad (67)$$

$$Re_k = \frac{u_k d_p \rho_g}{\mu} = 1,41 Ar^{0,56} , \quad (Ar > 10^4) \quad (68)$$

Ar number can be calculated with equation (58). Given this, $u_c = 2,75 \text{ m/s}$ and $u_k = 14,34 \text{ m/s}$. It is possible to state that for the velocities 3.3 m/s and 5.7 m/s, there is a turbulent regime, and for 0.9 m/s a bubbling regime.

The particle flow behaviors as the inlet air velocity increases of the experiments performed in the laboratory's pilot-scale fluidization unit are shown in Figure 24.

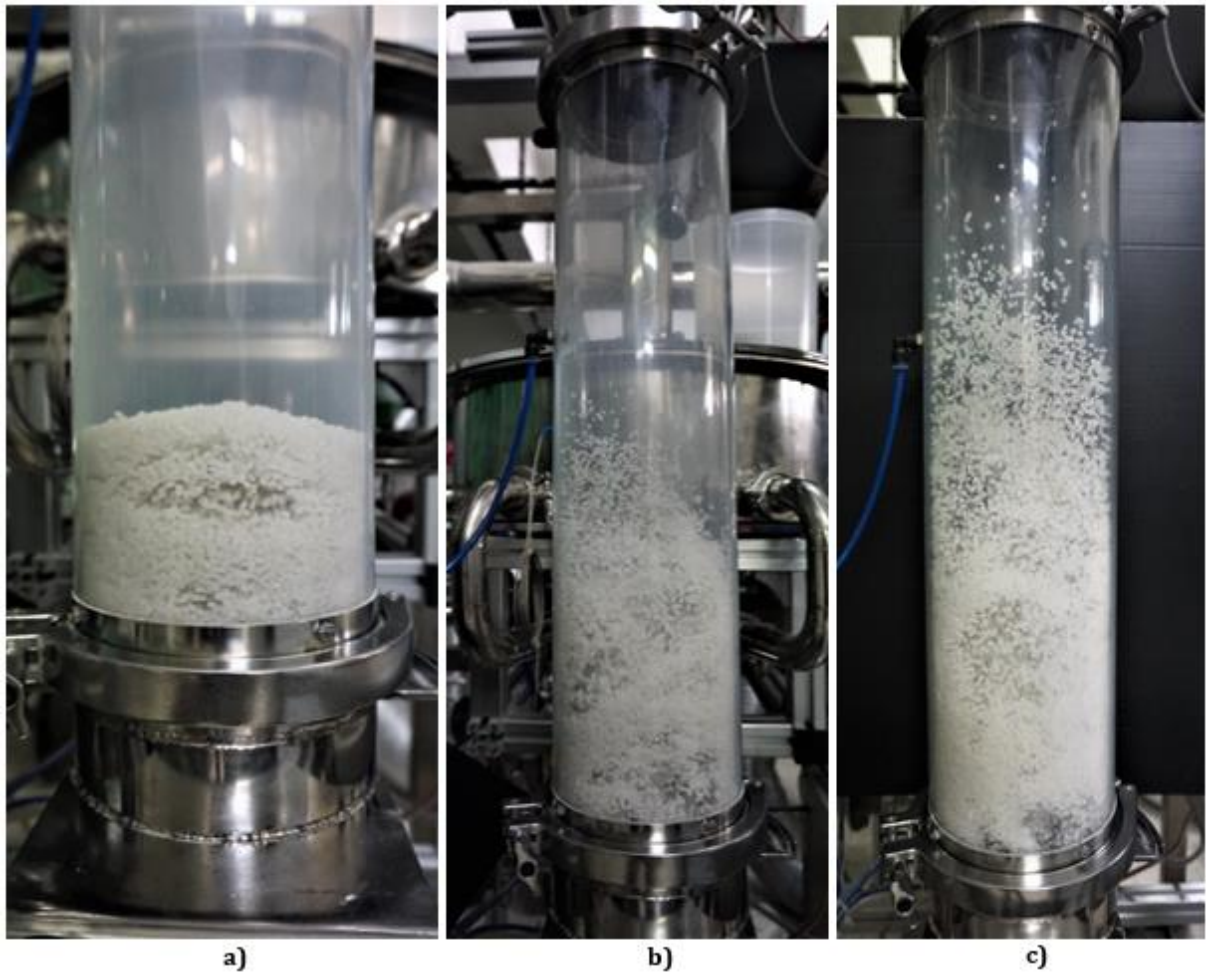


Figure 24- The particle flow behaviors for three different velocities performed in the faculty laboratory's pilot-scale fluidization unit. a) 0.9 m/s b) 3.3 m/s c) 5.7 m/s

Interpreting Figure 24, for the first situation, 0.9 m/s, there is practically no change in bed height and small bubbles. There is a bubbling regime. On the other hand, for the other two velocities, there is a turbulent regime, whereas in the c) situation, there is a more considerable bed expansion, and bubbles are not observed. This expansion of the bed is due to the higher velocity.

The average pressure drop for the experiment was 7 mbar, with an associated error of 18.85% compared to the theoretical value (5.89 mbar). The theoretical value was obtained from the classical equation (1) and (2).

The comparison of particle flow behavior between the experimental data recorded in the laboratory and the simulation at a turbulent regime is shown in Figure 25 and Figure 26.

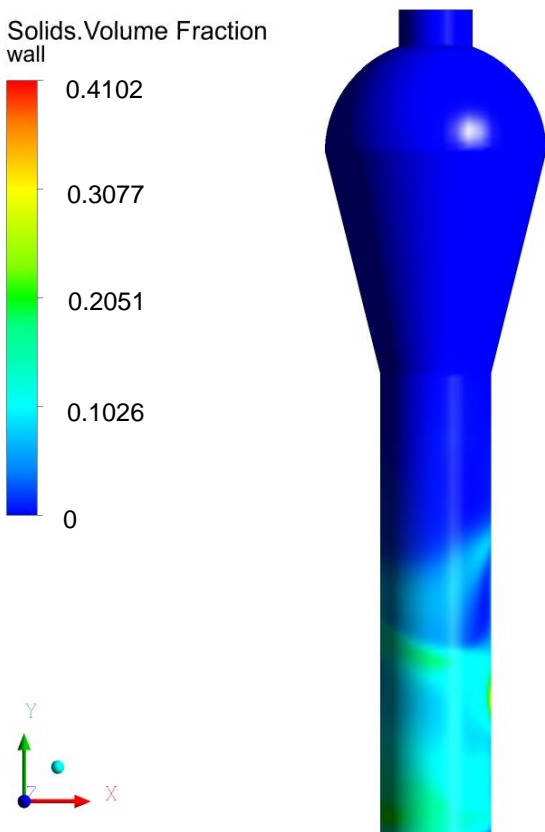
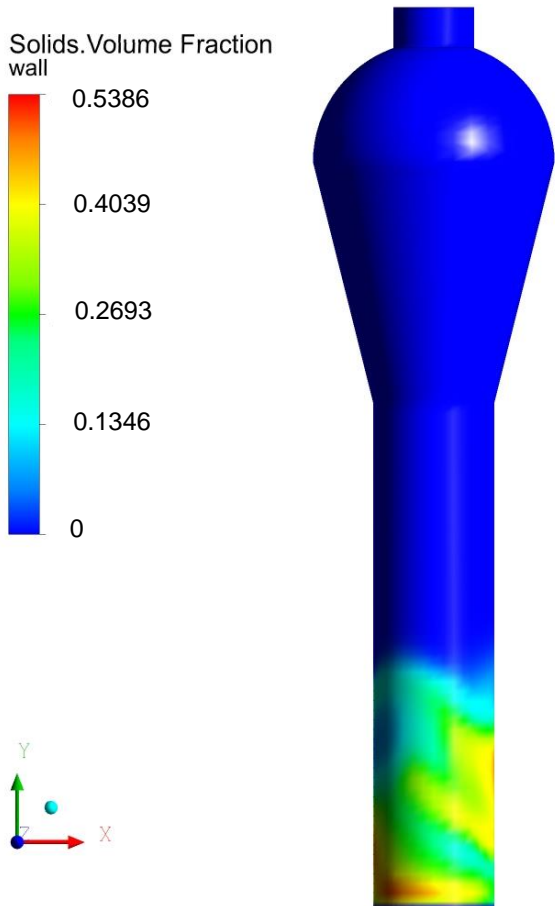


Figure 25- Simulation results of particle flow behavior compared with experimental particle flow behavior in the laboratory's pilot-scale fluidization, both at 3.3 m/s.

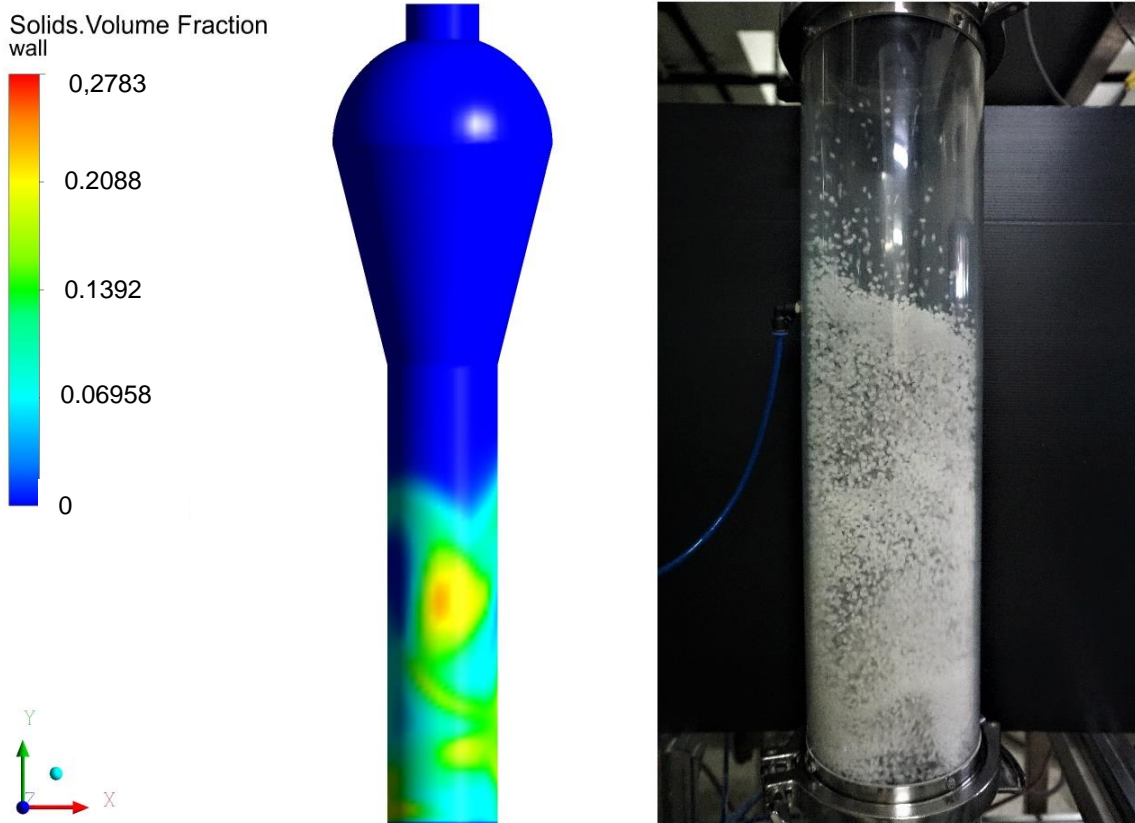


Figure 26- Results of particle flow behavior compared with experimental particle flow behavior in the laboratory's pilot-scale fluidization unit, both at 5.7 m/s.

From Figure 25 and Figure 26, the bed height can be observed along the particle bed in the y-axis. In both figures, it is possible to see a pattern in the particle flow behavior, and bed height is identical between the simulation and the laboratory's pilot-scale fluidization unit.

It is also possible to prove the fluidization regime, and there is a transition between the slugging fluidization and the turbulent fluidization for both situations. As expected, the bed height is higher in Figure 26, when the air velocity is higher.

It is possible to conclude that the developed model correctly predicts the particles' hydrodynamics.

Since the particles' hydrodynamics motion in an industrial-scale FBR is defined by the same computational models, and the CFD model has been validated experimentally in the description of pilot-scale particle flow behavior, it is possible to apply the same CFD model in the industrial-scale FBR simulation.

Applying the CFD model to an industrial-scale FBR allows performing virtual experiments that are difficult to perform in the actual system. The CFD analysis is crucial for performing scale-up design since material costs prohibit iterative experimentation.

5. RESULTS

5.1 CFD-PBM coupled model

The industrial-scale FBR was simulated with the 3D CFD-PBM model for about 250 s of real time simulation, to reach quasi steady state conditions. At the steady state fluidization condition, particles move vigorously inside the bed.

The u_{mf} is an essential hydrodynamic parameter in the design of an FBR since it determines the transition of fixed bed into a fluidized bed, and at higher velocities, quantifies the intensity of the fluidization regime.

The u_{mf} is 0.38 m/s in order to fully and steadily fluidize the solid mixtures.

In the beginning, all the particles are stagnant since the velocity is lower than u_{mf} . With the increase of the gas velocity, the bed pressure drop steps up along the bed. Later, with the increasing of the gas velocity, the pressure drop decreases as small particles begin to fill the voids between coarse particles. Coarse particles remain unchanged.

Figure 27 shows the existence of two stages of flow regime with increasing gas velocity to show the sensitivity of the fluidization process to u_{mf} .

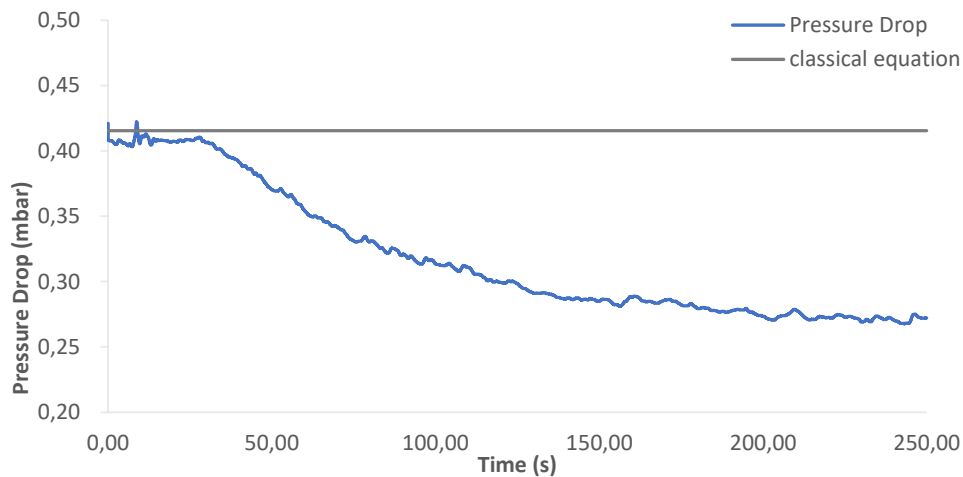


Figure 27- Transient fluidization. Pressure drop in function of time in an industrial-scale FBR with a CFD-PBM simulation. Classical value of 0.4153 bar from classical equation (1) and (2), calculated in **C.2. Grid for industrial-scale FBR**

First, from 0 to 30 s, the velocity is less than u_{mf} . The two initially well-mixed phases should not be separated. Thus, the particles remain in a fixed bed condition with nearly constant pressure drop (around 0.40 mbar) and void fraction, resulting in a homogeneous flow pattern. As the velocity increases, Figure 28, it starts to observe the fluidization of particles in a well-mixed condition, promoting contact between the catalyst particles with the monomer.

As the reaction begins, the particle size in the reactor increases. Considering the pressure drop equations (1) and (2), pressure loss could be expected to increase with the increasing

volume fraction of solids. However, there is a decrease in pressure drop due to the decrease in particle fraction inside the reactor. Since the velocity chosen for the simulation is higher than the terminal velocity of the initial particles, they soon leave the reactor. About 30% of the initial solid was lost. This phenomenon is represented between 30 s and 210 s, shown in Figure 27.

However, the pressure drop across the bed decreases to a constant value, which represents the fixed bed fluidization structure, 210s to 250s. Smaller particles have either left the reactor or have reached a sufficient size for fluidization.

During the simulation time, the superficial gas velocity gradually increases, as shown in Figure 28.

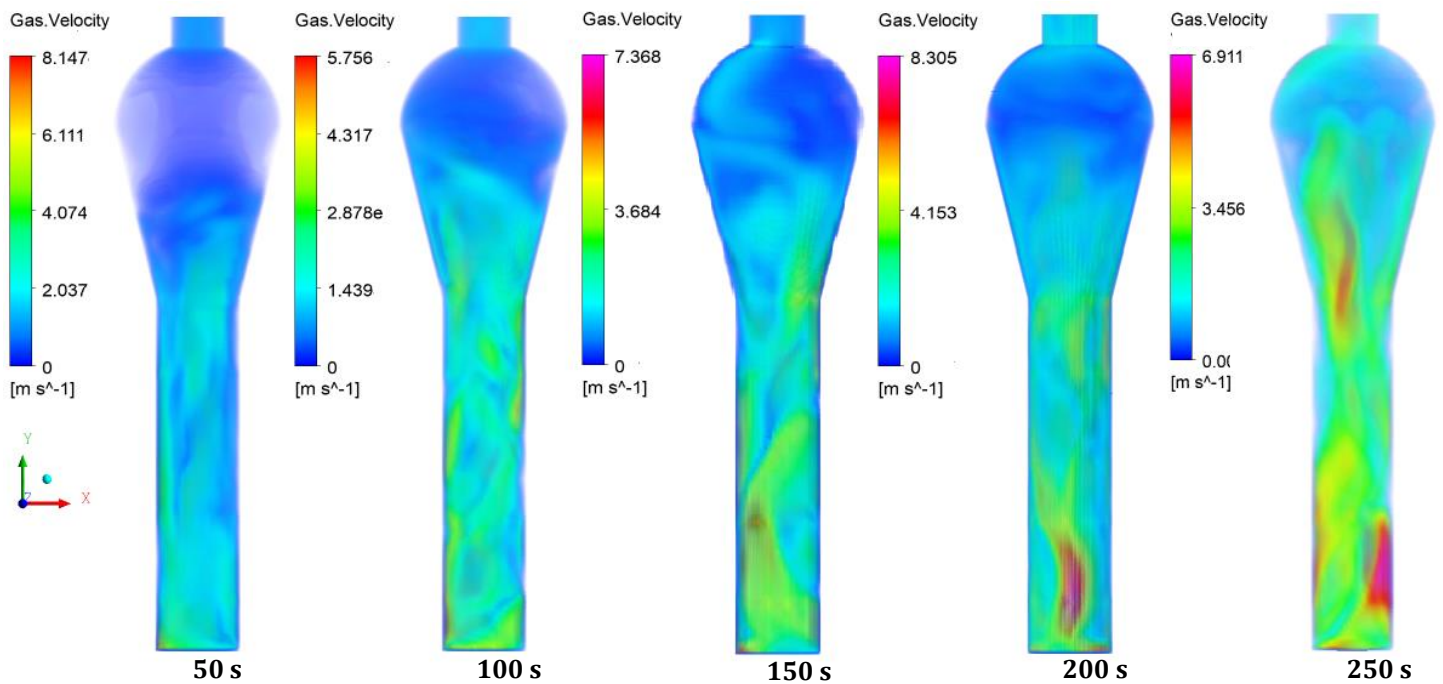


Figure 28- Volume rendering of gas velocity in an industrial-scale FBR with a CFD-PBM simulation.

In Figure 28 it is possible to verify that in the disengagement zone, the gas has a lower velocity. This decrease in velocity is due to the increased section area.

Comparing Figure 28 with Figure 29, it can be seen that along the reaction and freeboard zone, the gas has a higher velocity in the zones that have the smallest volume solids fraction.

However, as the velocity increases, the fluidization regime changes.

Knowing the properties of the particles, Table 8, in **Appendix A – Particle classification** it was found that the particles belong to group B. Thus, the equations to calculate the minimum velocities for each regime are the same used for particles of group D. As shown above, for group D and B particles, the u_{mb} is equal to the u_{mf} , 0.128 m/s. Using the equation (66), u_{sl} was calculated, which has a value of 0.618 m/s. The velocity used is between these two velocities, so it is bubbling fluidization.

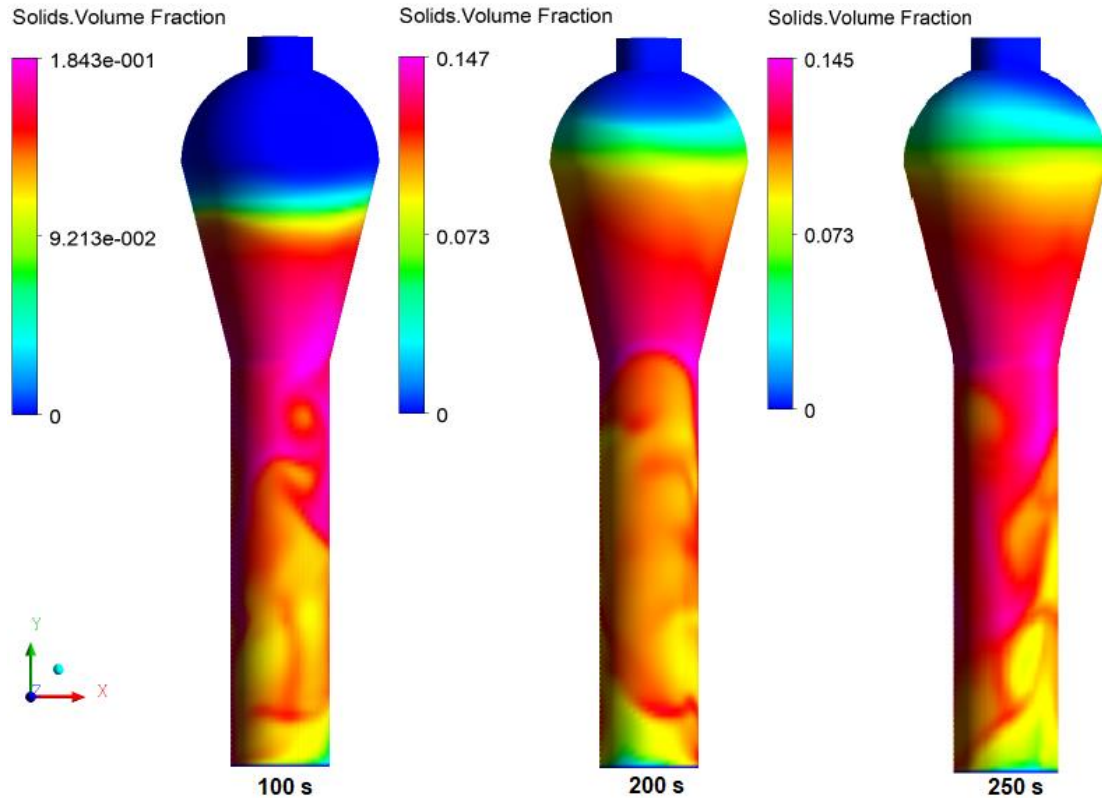


Figure 29 - The evolution of solid volume fraction contour in an industrial-scale FBR with a CFD-PBM simulation.

Figures 30 and 31 represent the solids velocity and the volume fraction of solids along the reactor height with some fluctuations.

The velocity at the reactor inlet is higher since the solids fraction is otherwise smaller. Firstly, the particle velocities reduce, and then increase but finally decrease to zero. That is, from that moment onwards, there is a progressive increase in velocity, and around 20 m high, there is a break. At about this point, the velocity begins to decrease gradually. This is because it is around 20 m that the disengagement zone begins.

The bed height between 50 s, and 150s and 250s are significantly different, but between 200s and 250 s is not a pronounced difference. This small difference is justified by the fact that a stable fluidization state has been reached.

At 50 s, there are no solids at the top of the reactor, while at 200s and 250s, solids are present, although a minimal percentage. This indicates that as the reaction proceeds, particles will exit through the reactor outlet.

Comparing the three situations, at 50 s, there is a higher solids volume fraction because the bed expansion is smaller, which leads to a higher concentration of solids.

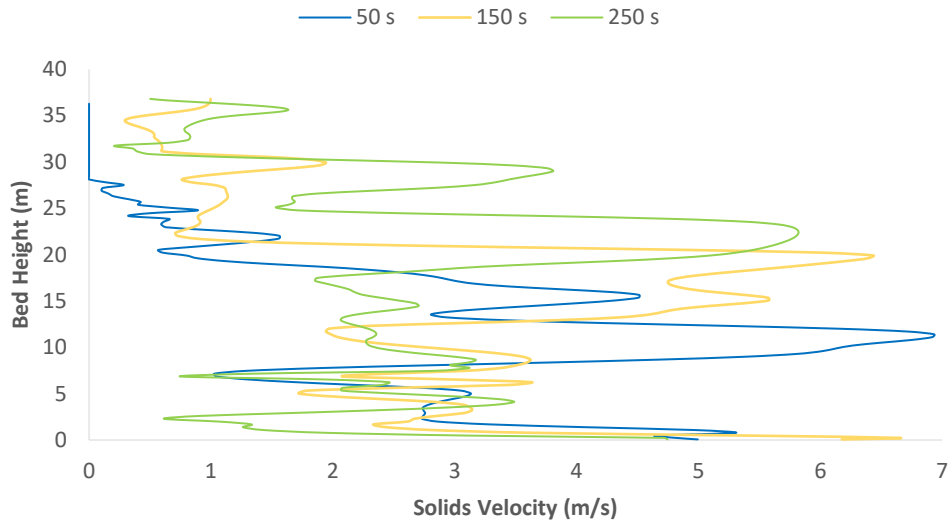


Figure 30- The time-averaged solid velocity for each plan along the bed height in an industrial-scale FBR with a CFD-PBM simulation.

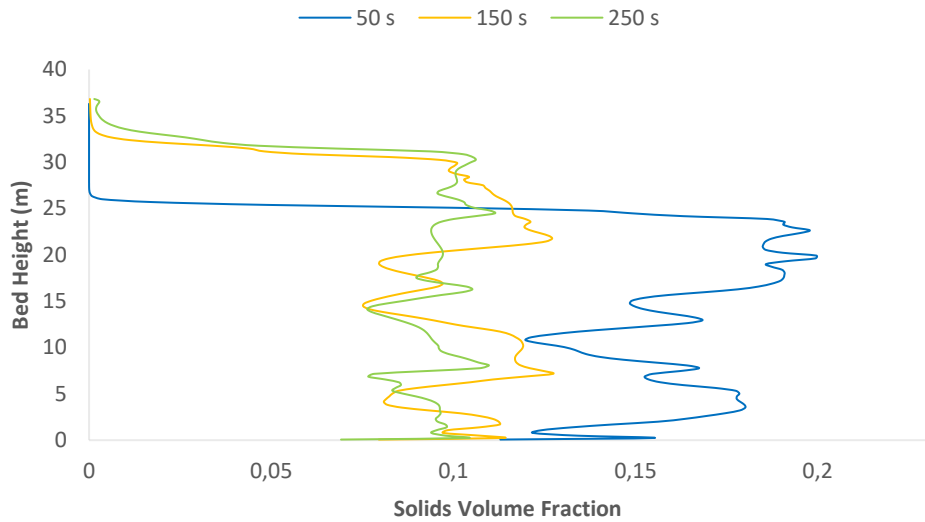


Figure 31- The time-averaged solid volume fraction for each plan along the bed height in an industrial-scale FBR with a CFD-PBM simulation.

Figure 32 shows the time-averaged solid velocities and volume fraction along the radial directions in the different heights inside the reactor.

In FBRs, it is quite common to find a typical flow structure consisting of two regions, the center-dilute core region, and the wall-dense annulus region. [29] The first one consists of a dilute upward-flowing suspension of solids, and the second one in the dense downward-flowing suspension of solids. Solid particle velocity and solid holdups can reveal these regions.

In Figure 32 b) can be seen a dilute-gas solid core in the center and a surrounding high solid volume fraction annular region near the wall.

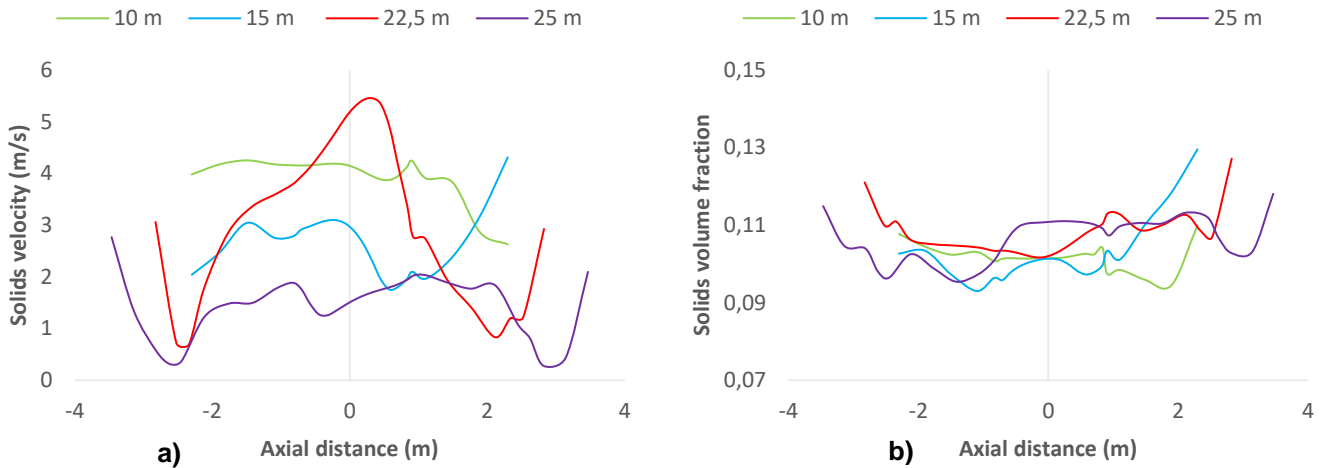


Figure 32- The particle velocity profile along the radial direction (a) and the mean solid volume fraction along the radial direction (b) at 250 s in an industrial-scale FBR with a CFD-PBM simulation.

Figure 32 a) shows the time-averaged axial particle velocity at each height of the vertical bed region. The particle velocity is inversely related to the solid volume fraction [47], as shown in $v_s = W_s / \rho_s \varepsilon_s$ where W_s is the solid flux ($\text{kg}\cdot\text{m}^{-3}\cdot\text{s}^{-1}$), ρ_s is solid density ($\text{kg}\cdot\text{m}^{-3}$), and ε_s is the solid volume fraction. The higher the solid volume fraction, the lower the velocity.

Figure 33 shows that during the simulation, the central zone in the vertical section of the reactor bed has lower solid volume fraction values, which confirms what was said above. This accentuation of the distinction between the two regions over time is because it is approaching an ideal fluidization state.

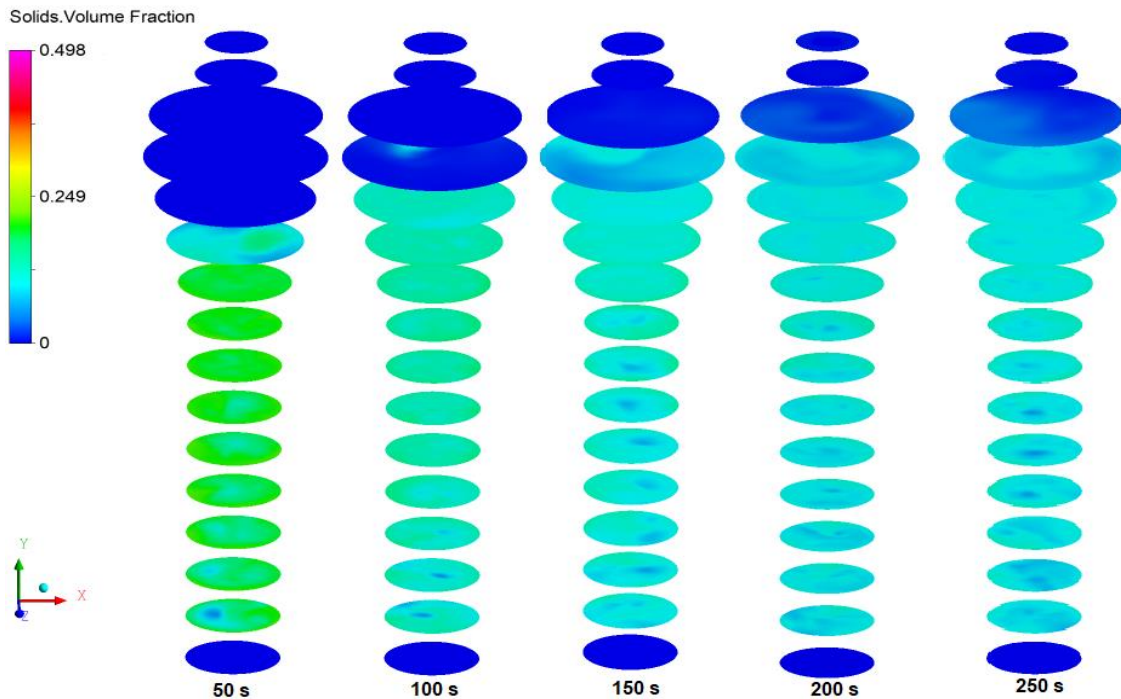


Figure 33- The evolution of solid volume fraction contour in the reactor for different heights in an industrial-scale FBR with a CFD-PBM simulation.

It is necessary to obtain a fundamental understanding of the temperature distribution in the bed since a temperature field can reflect the state of fluidization and helps verify the bed operating status. Since the ethylene polymerization reaction is extremely exothermic, it is necessary to remove the produced heat as quickly and efficiently as possible.

Figure 34 shows the mean temperature profiles for different simulation times.

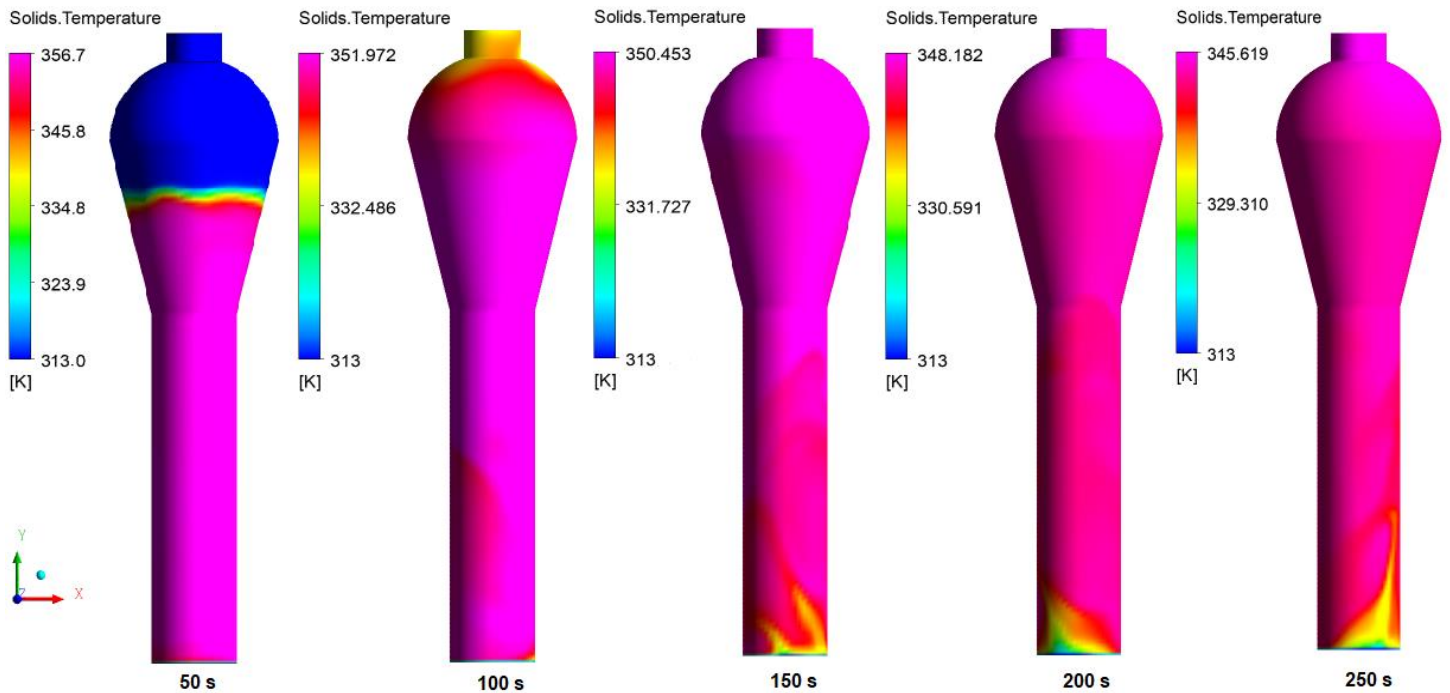


Figure 34- The evolution of solids temperature contour in an industrial-scale FBR with a CFD-PBM simulation.

The industrial-scale FBR presents a non-uniform bed temperature.

There is a temperature decrease within the reactor as the initial solids temperature set was 363K, and the gas temperature at the reactor inlet is 313K. The solids temperature gradually cools down.

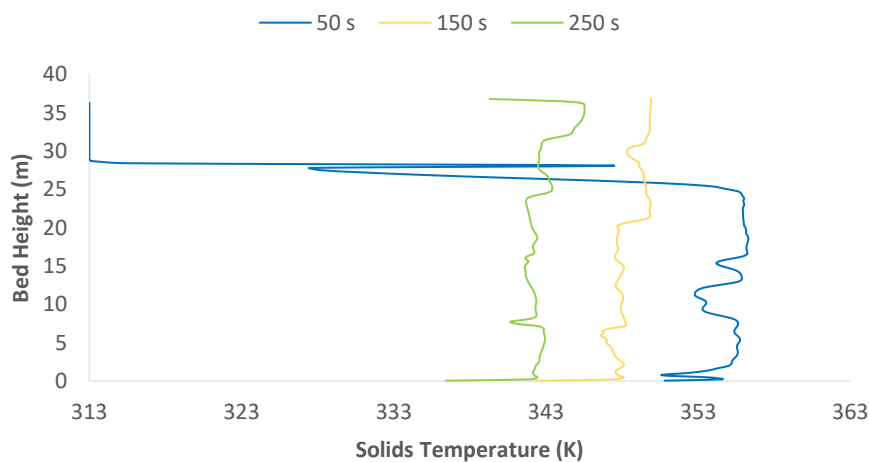


Figure 35- The time-averaged solids temperature along the bed height in an industrial-scale FBR with a CFD-PBM simulation.

In Figure 35, it is possible to check the temperature fluctuations in the reactor for different simulation times.

In the upper region of the bed, the temperature profiles present higher values, Figure 36 and Figure 35, than in the other bed regions. This occurs because, in the disengagement region, the convective heat transfer dominates the formation of temperature profiles in the growing particles. Nevertheless, the temperature variations also depend on the gas phase temperature.

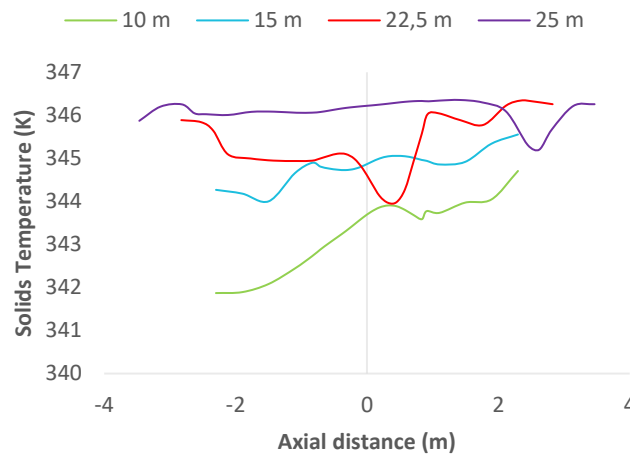


Figure 36- Solids temperature profile along the radial direction at 250 s in an industrial-scale FBR with a CFD-PBM simulation.

The particle growth rate effect is considered because it is directly related to the polymerization kinetics. The particle size distribution is shown in term of the length number density, which represent the number of solid particles in the unit of volume of the reactor per unit particle diameter (m^3/m). The growth rate equation (58), is valid in the range of particle diameter $0 \leq L \leq 0.0012 m$ [11][6][48].

In this dissertation, the mean particle diameter reached is $545.1 \mu m$ using the simulation time of 250 s, and an initial mean diameter of $200 \mu m$. The average particle diameter as a function of time is shown in Figure 37.

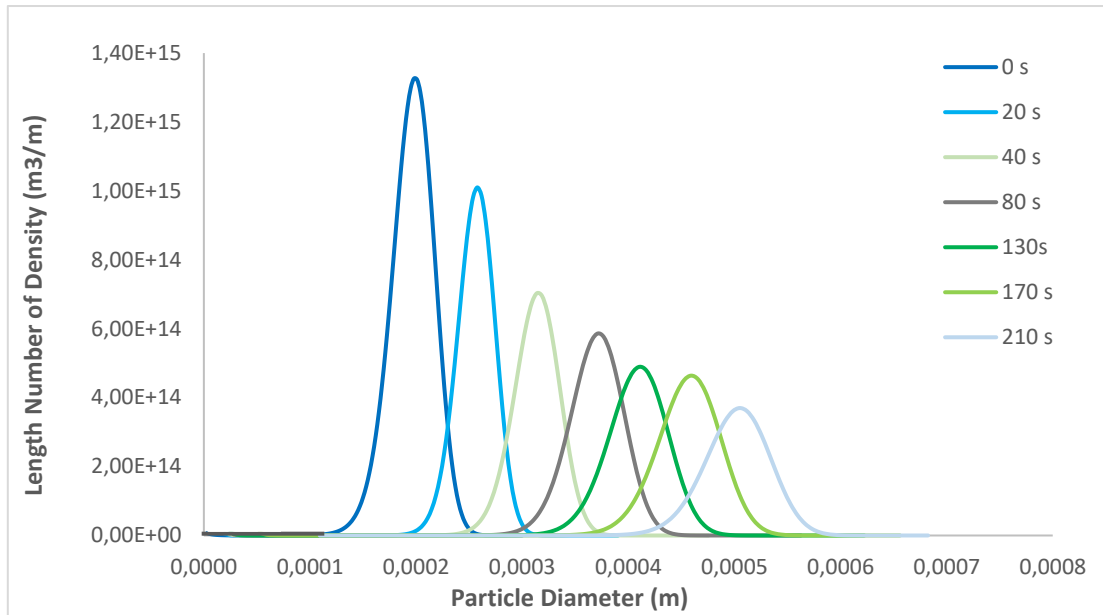


Figure 37- The particle size distribution due to the growth rate in an industrial-scale FBR with a CFD-PBM simulation.

The particle growth rate of particles in the industrial-scale FBR is approximately $1.62 \mu\text{m/s}$. The calculation of this value is explained in **Appendix D – Particle growth rate**.

The particle size progressively grows as the polymerization time increases. The particle distribution shows flatter as the particles grow due to more uniformity of particle size.

Based on equation (58), one can predict that the growth rate of smaller particles is faster than that of larger particles. With the polymerization proceeding, the uniformity of particle sizes in the reactor increases and then the PSD gets broader. Therefore, the PBM coupled with the CFD model, can be used to describe the particle growth.

6. CONCLUSIONS AND FUTURE WORK

In this work, a 3D CFD-PBM couple model was developed to describe the gas-solid two-phase flow in an industrial-scale FBR, utilizing ANSYS Fluent software.

First, a 3D CFD model was developed to study the cold-flow behavior of PE particles in a pilot-scale fluidization unit. The 3D CFD model incorporates the Eulerian-Eulerian two-fluid model, KTGF, and turbulence model.

For the model validation, the pressure drop from the simulation results and the experimental pressure drop were compared with the pressure drop calculated through empirical equations, 5.89 mbar. The simulation and laboratory experiment were performed for two different velocities, $4u_{mf} = 3.3 \text{ m/s}$ ($Re=870$), and $7u_{mf} = 5.7 \text{ m/s}$ ($Re=1520$), during 6s real-time simulation. A pressure drop of 7 mbar and 5.91 mbar were obtained for the experimental and simulation results, respectively. There is an error of 0.34% for the simulation result, and 18.85% in the experimental result.

Although the simulation error to the theoretical value is practically nil, it is necessary to understand what may have affected the experiment since the error between the experimental and theoretical value is considerable. The device indicating the reactor pressure drop only shows the value of the units. Given the order of magnitude of the values concerned, this aspect has a significant influence on the result. Another aspect to be considered regarding the accuracy of the results is that the laboratory reactor is constantly opened and dismantled for experiments. Because of this, the sensors may be affected and influence the displayed value.

In the model validation, an analysis of the bed height can also be done. The flow behaviors were compared, verifying a transitional regime between slugging and turbulent, and the simulation results are consistent with the experimental data.

Subsequently, population balance, polymerization heat, and polymerization kinetics were incorporated into the validated model in order to develop a 3D CFD-PBM model for an industrial-scale FBR.

The 3D CFD-PBM coupled model was preliminarily tested by comparing the simulated results with the classical calculated data.

The simulation was performed for a velocity of $3u_{mf} = 0.38 \text{ m/s}$ ($Re=769$) during 30 s of real time simulation, obtaining a pressure drop of 0.4085 bar. Comparing this value with the value obtained through empirical equations, 0.4153 bar, an error of 1.65% is verified. Thus, the model can represent the actual behavior of real mixture with reasonable accuracy in terms of pressure drop.

Finally, the distinguished model was used to study the PE particle flow patterns and temperature field.

The results show that the pressure drop across the bed decreases to a constant value, which represents the fixed bed fluidization structure. In the first stage, the particles remain in a fixed bed condition with nearly constant pressure drop (around 0.40 mbar) and void fraction, resulting in a homogeneous flow pattern. As the velocity increases, it starts to observe the fluidization of particles in a well-mixed condition, promoting the reaction beginning. The particle size in the reactor increases, and the bed voidage also increases. As pressure drop is inversely related to void fraction, the pressure drop decreases.

The temperature of solid-phase increases from the bottom to the top of FBR since, in the disengagement zone, the convective heat transfer dominates the formation of temperature profiles in the growing particles. The simulated results also show that the inlet gas velocity is an essential factor in controlling the reactor temperature fields, verifying a decrease in reactor temperature over time. Thus, the industrial-scale FBR presents a non-uniform bed temperature.

Given the importance of the reactor temperature profile, several studies have been carried out to find a solution to improve this aspect. One option is to use rotating FBRs since that allows a uniform bed temperature [49]. However, this type of reactor is not yet used to produce PE at the industrial-scale.

The particle growth rate of the industrial scale FBR is approximately $1.62 \mu\text{m}/\text{s}$, obtaining a final average particle diameter of $545.1 \mu\text{m}$. However, in this work, the effect of aggregation and breakage was not considered. It was only considered the particle growth, adopting a kinetics model containing the mainly elementary chain propagation reaction. Thus, future work consists of the use of a comprehensive kinetic model, considering all the elementary reactions of PE polymerization process, species transport for gas and solid phase, and scalar transport. This will allow better accuracy regarding the PSD and flow behavior inside the reactor.

It is possible to conclude that the 3D CFD-PBM developed coupled model is not only appropriated to accurate simulate the flow behavior and PSD, but also brings together all the features presented in past articles applied on a 3D industrial-scale FBR. The 3D CFD-PBM model allows optimizing operating conditions and equipment design, leading to improved process safety and process efficiency, and decreasing capital and operating costs.

7. REFERENCES

- [1] Ronca, S. (2016). Polyethylene. In *Brydson's Plastics Materials: Eighth Edition*. 10, 247- 277.
- [2] Beroe Inc. (2018). Category intelligence on ethyl acetate.
- [3] Patel, Rajen M. (2016). Polyethylene. In *Multilayer Flexible Packaging: Second Edition*. 2, 17-34.
- [4] Production, P. (n.d.). TECHNOLOGIES POLYETHYLENE PRODUCTION TECHNOLOGIES POLYETHYLENE PRODUCTION TECHNOLOGIES ROUTES TO.
- [5] Htu, T. C. M. (n.d.). Production of Polyethylene Using Gas Fluidized Bed Reactor. 1–20.
- [6] Akbari, V., Nejad, T., Borhani, G., Shamiri, A., Kamaruddin, M., & Hamid, A. (2015). 2D CFD-PBM simulation of hydrodynamic and particle growth in an industrial gas phase fluidized bed polymerization reactor. In *Chemical Engineering Research and Design* (Vol. 104).
- [7] Che, Y., Tian, Z., Liu, Z., Zhang, R., Gao, Y., Zou, E., ... Liu, B. (2015). CFD prediction of scale-up effect on the hydrodynamic behaviors of a pilot-plant fluidized bed reactor and preliminary exploration of its application for non-pelletizing polyethylene process. *Powder Technology*, 278, 94–110.
- [8] Chen, X., Luo, Z., Yan, W., Lu, Y., & Ng, I. (2011). Three-Dimensional CFD-PBM Coupled Model of the Temperature Fields in Fluidized-Bed Polymerization Reactors (Vol. 57).
- [9] Akbari, V., Nejad Ghaffar Borhani, T., Shamiri, A., & Kamaruddin Abd. Hamid, M. (2015). A CFD-PBM coupled model of hydrodynamics and mixing/segregation in an industrial gas-phase polymerization reactor. In *Chemical Engineering Research and Design* (Vol. 96).
- [10] Che, Y., Tian, Z., Liu, Z., Zhang, R., Gao, Y., Zou, E., ... Liu, B. (2016). An Insight into the Temperature Field and Particle Flow Patterns in a Fluidized Bed Reactor for Nonpelletizing Polyethylene Process Using a 3D CFD-PBM Model. In *Industrial and Engineering Chemistry Research* (Vol. 55).
- [11] Yan, W., Luo, Z., Lu, Y., & Chen, X. (2012). PARTICLE TECHNOLOGY AND FLUIDIZATION A CFD-PBM-PMLM Integrated Model for the Gas – Solid Flow Fields in Fluidized Bed Polymerization Reactors (Vol. 58).
- [12] Yao, Y., Su, J., & Luo, Z. (2015). CFD-PBM modeling polydisperse polymerization FBRs with simultaneous particle growth and aggregation: The effect of the method of moments. In *Powder Technology* (Vol. 272).

- [13] (2019, April) Polyethylene. [online] <https://pslc.ws/macrog/pe.htm>.
- [14] Lazonby, J., Poly(ethene) (Polyethylene). [online] <http://www.essentialchemicalindustry.org/polymers/polyethene.html>.
- [15] A.J.Peacock. (2000). Handbook of Polyethylene: Structures:Properties and Applications (1st ed.). CRC Press.
- [16] Polyethylene. [online] <https://www.britannica.com/science/polyethylene>
- [17] D. B. Maspas. (2010). Industrial Polyethylene: Properties, Catalyst, Processes. Wiley.
- [18] Polyethylene (PE). [online] <https://omnexus.specialchem.com/selection-guide/polyethylene-plastic>.
- [19] J. B. P. Soares & T. F. L McKenna (2012). Polyolefin Reaction Engineering. Wiley-VCH.
- [20] Zhou, Y., Wang, J., Yang, Y., & Wu, W. (2013). Modeling of the Temperature Profile in an Ethylene Polymerization Fluidized-Bed Reactor in Condensed-Mode Operation.
- [21] Kiashemshaki, A., Mostoufi, N., & Sotudeh-gharebagh, R. (2006). Two-phase modeling of a gas phase polyethylene fluidized bed reactor. 61, 3997–4006.
- [22] Escola Politécnica da USP Departamento de Engenharia Química (2013). OPERAÇÕES UNITÁRIAS DA INDÚSTRIA QUÍMICA - FLUIDIZAÇÃO.
- [23] Soares, J. B. P., & McKenna, T. F. L. (2012). Polymerization Catalysis and Mechanism. In Polyolefin Reaction Engineering (pp. 53–86).
- [24] Yan, W., Luo, Z., Lu, Y., & Chen, X. (2012). PARTICLE TECHNOLOGY AND FLUIDIZATION A CFD-PBM-PMLM Integrated Model for the Gas – Solid Flow Fields in Fluidized Bed Polymerization Reactors (Vol. 58).
- [25] Jubsilp, C., Takeichi, T., & Rimdusit, S. (2011). Polymerization kinetics. Handbook of Benzoxazine Resins, 157–174.
- [26] Abbasi, M. R., Shamiri, A., & Hussain, M. A. (2016). Dynamic modeling and Molecular Weight Distribution of ethylene copolymerization in an industrial gas-phase Fluidized-Bed Reactor. Advanced Powder Technology, 27(4), 1526–1538.
- [27] Geraldés, V. (2017). Dinâmica de Fluidos Computacional [Powerpoint slides].
- [28] Pan, H., Liang, X. F., & Luo, Z. H. (2016). CFD modeling of the gas–solid two-fluid flow in polyethylene FBRs: From traditional operation to super-condensed mode. Advanced Powder Technology, 27(4), 1494–1505.

- [29] Che, Y., Tian, Z., Liu, Z., Zhang, R., Gao, Y., Zou, E., ... Liu, B. (2015). A CFD-PBM model considering ethylene polymerization for the flow behaviors and particle size distribution of polyethylene in a pilot-plant fluidized bed reactor. *Powder Technology*, 286, 107–123.
- [30] Yao, Y., He, Y. J., Luo, Z. H., & Shi, L. (2014). 3D CFD-PBM modeling of the gas-solid flow field in a polydisperse polymerization FBR: The effect of drag model. *Advanced Powder Technology*, 25(5)
- [31] Chen, X. Z., Shi, D. P., Gao, X., & Luo, Z. H. (2011). A fundamental CFD study of the gas-solid flow field in fluidized bed polymerization reactors. *Powder Technology*, 205(1–3), 276–288
- [32] Dehnavi, M. A., Shahhosseini, S., Hashemabadi, S. H., & Ghafelebashi, S. M. (2010). CFD simulation of hydrodynamics and heat transfer in gas phase ethylene polymerization reactors. *International Communications in Heat and Mass Transfer*, 37(4), 437–442.
- [33] C.K.K. Lun, S.B. Savage, D.J. Jeffrey, N. Chepur, (1984). Kinetic theories for granular flow-inelastic particles in Couette-flow and slightly inelastic particles in a general flow field, *J. Fluid Mech.* 140, 223-256.
- [34] J. Ding, D. Gidspow, (1990). A bubbling fluidization model using kinetic-theory of granular flow, *AIChE J.* 36(4)
- [35] M. Syamlal, W. Rogers, T.J. O'Brien (1993) *MFIX Documentation: Volume 1, Theory Guide*, National Technical Information Service (Vol.1).
- [36] Gómez, G. C. (2012). *Dinámica de Fluidos Computacional Dinámica de Fluidos Computacional*.
- [37] Chen, X., Luo, Z., Yan, W., Lu, Y., & Ng, I. (2011). *Three-Dimensional CFD-PBM Coupled Model of the Temperature Fields in Fluidized-Bed Polymerization Reactors (Vol. 57)*.
- [38] Akbari, V., Borhani, T. N. G., Godini, H. R., & Hamid, M. K. A. (2014). Model-based analysis of the impact of the distributor on the hydrodynamic performance of industrial polydisperse gas phase fluidized bed polymerization reactors. *Powder Technology*, 267, 398–411.
- [39] Gidaspow D. (1994) *Multiphase Flow and Fluidization: Continuum and Kinetic Theory Descriptions*. Boston: Academic Press.
- [40] Soares, J. B. P., & McKenna, T. F. L. (2012). Particle Growth and Single Particle Modeling. *Polyolefin Reaction Engineering*, 271–309.
- [41] Anantharaman, A., Cocco, R. A., & Chew, J. W. (2018). Evaluation of correlations for minimum fluidization velocity (U_{mf}) in gas-solid fluidization. *Powder Technology*, 323, 454–485.

- [42] Caminha, G. (2019). The CFL Condition and How to Choose Your Timestep Size. SIMSCALE [online] <https://www.simscale.com/blog/2017/08/cfl-condition/>
- [43] (2009). 26.4.1 Changing the Courant Number. ANSYS [online] <http://www.afs.enea.it/project/neptunius/docs/fluent/html/ug/node789.htm>
- [44] Bakker, A.(2006). Lecture 7- Meshing. [online] <http://www.bakker.org/dartmouth06/engs150/07-mesh.pdf>
- [45] G. Anzaldo Muñoz (2015) MESH QUALITY AND ADVENCED TOPICS ANSYS WORKBENCH 16.0. [online] https://www.academia.edu/16970000/MESH_QUALITY_AND_ADVENCED_TOPICS_ANSYS_WORKBENCH_16.0?auto=download
- [46] Basu, P. (2015). Circulating fluidized bed boilers: Design, operation and maintenance. In Circulating Fluidized Bed Boilers: Design, Operation and Maintenance.
- [47] Dfg - M. Kashyap, D. Gidaspow,W.J. Koves, (2011). Circulation of Geldart D type particles: part I —high solids fluxes. Measurements and computation under solids slugging conditions, Chem. Eng. Sci. 66, 183–206
- [48] Ahmadzadeh, A., Arastoopour, H., Teymour, F., & Strumendo, M. (2008). Population balance equations' application in rotating fluidized bed polymerization reactor. Chemical Engineering Research and Design, 86(4), 329–343.
- [49] de Broqueville, A., & De Wilde, J. (2009). Numerical investigation of gas-solid heat transfer in rotating fluidized beds in a static geometry. Chemical Engineering Science, 64(6), 1232–1248.

Appendix A – Particle classification

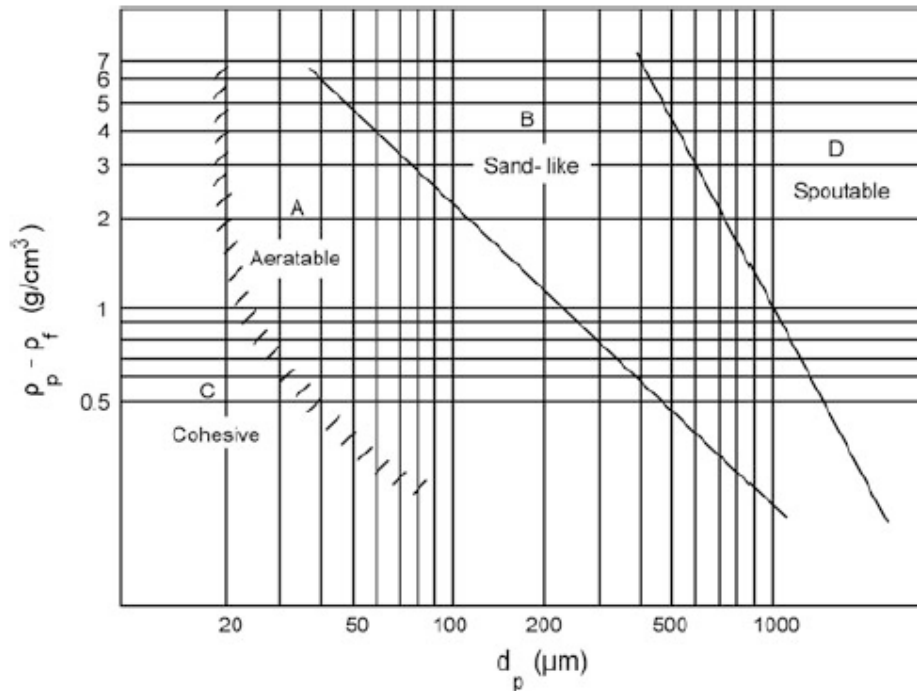


Figure 38-Powder classification of granular solids. [21]

Taking into consideration the properties of the particles present in Table 6 and Table 8, it is possible to classify the particles. Geldart classified solids broadly under four groups, A, B, C, and D, as shown in Figure 38. This classification is essential to understand the fluidization behavior of solid particles. Under similar operating conditions, particles of different groups may behave entirely differently.

Table 11- Particles classification

	$\rho_s - \rho_g$	d_p	Group
A.1	0.952	2500 μm	D
A.2	0.83	1200 μm	B

Appendix B – Pilot-scale reactor dimensions

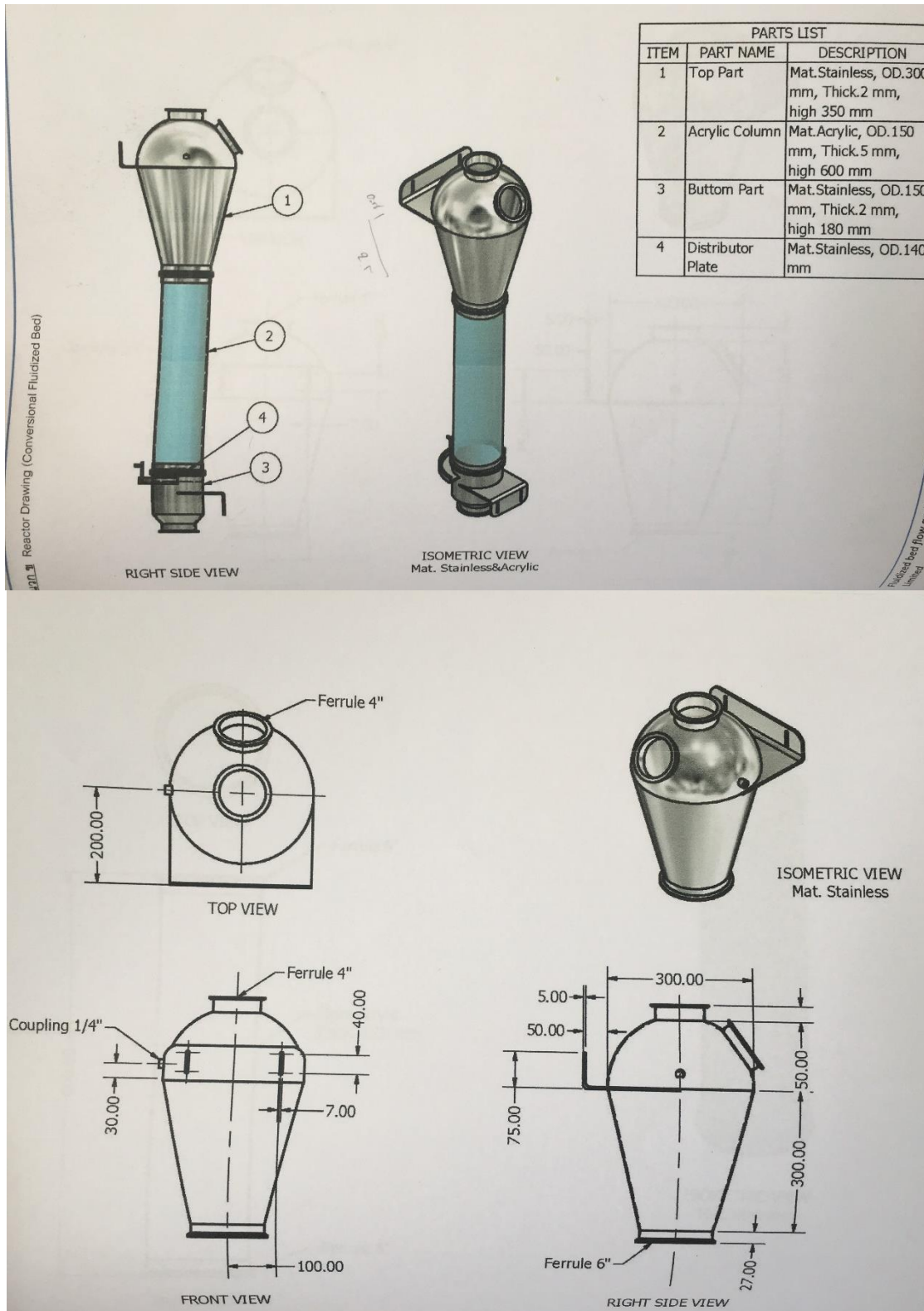


Figure 39- Design of the pilot-scale reactor provided by the manufacture

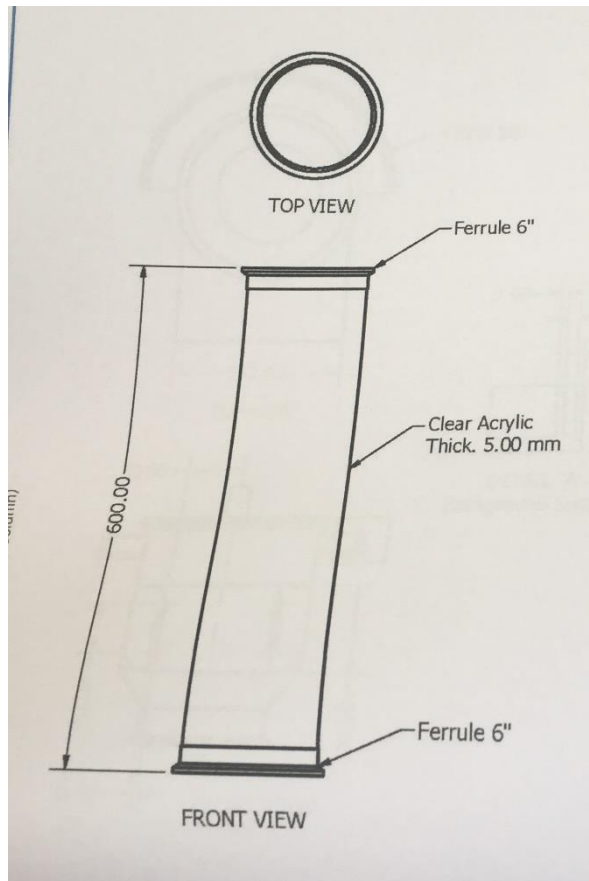


Figure 40- Design of the pilot-scale reactor provided by the manufacture

Appendix C – Sensitivity analysis of grid

C.1. Grid for pilot-scale fluidization unit

The current study focuses on finding a suitable number of cells that are adequate to predict the hydrodynamics in the pilot-scale fluidization unit and provide grid-independent results. The grid has a significant impact on the rate of convergence, solution accuracy, and CPU time required. Therefore, the mesh quality is essential to get reasonable solutions. In Table 4, it is possible to see the nodes number and quality parameters for the pilot-scale fluidization unit meshes.

CFD simulated pressure drop data was compared with the classical calculated data according to the empirical equation (1) and (2), $\Delta P = 5.89 \text{ mbar}$, and the experimental value obtained from the pilot-scale fluidization unit of the laboratory, $\Delta P = 7 \text{ mbar}$, for a simulation real time of 6 s as shown in Figure 41.

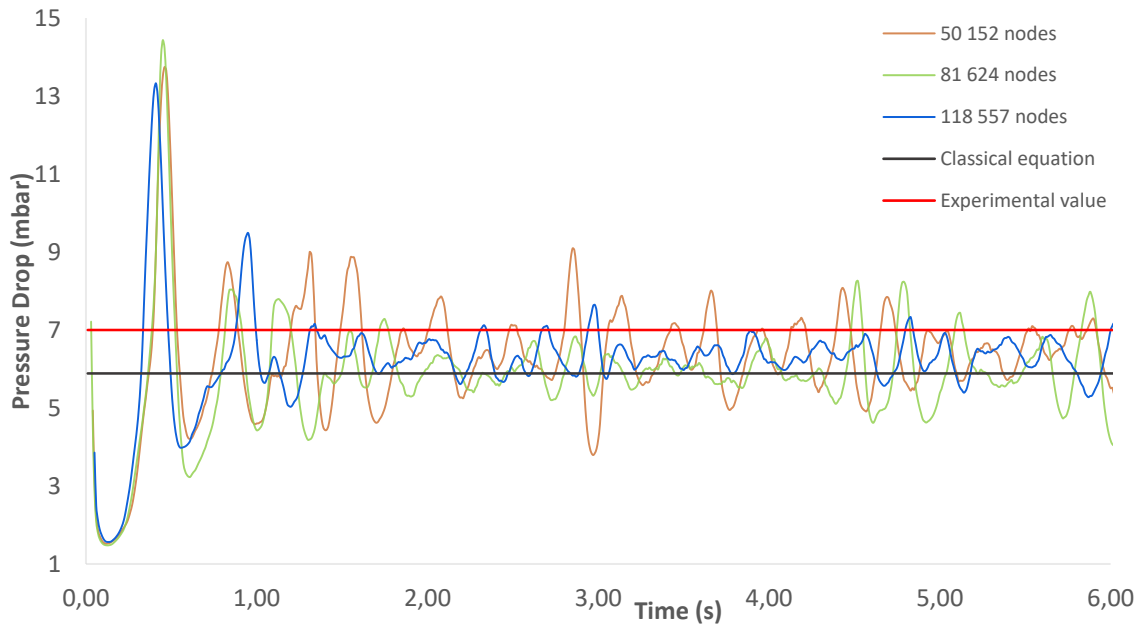


Figure 41-The pressure drop as a function of flow time using different grids in a pilot-scale fluidization unit with a CFD simulation. ($v_g=3.3 \text{ m/s}$). The theoretical value of 5.89 mbar from classical equation (1) and (2), and the experimental value of 7 mbar from the experiment in the laboratory's pilot-scale fluidization unit.

Regard Figure 41, the simulated results meet the data from the classical model well. For the three distinct situations, the simulated values are very close to those of the classical equations, (1) and (2), and the value verified experimentally. There are small oscillations, whereas the mesh with 118 557 nodes has the lowest oscillation. It is possible to identify two regions, the start-up ($t < 1\text{s}$) and stable fluidization stages. The maximum bed pressure drop at the start-up stage is around 13-14 mbar, much higher than at the stable stage. This occurs since it is necessary to overcome the inter-particle locking. After this first stage, the bed pressure drop

fluctuates with time around the value given by the empirical equation (1) and (2). The simulated pressure drop values fluctuations are due to the violent motions of particles in the actual bed.

The pressure drop along the fluidization unit is depicted in Figure 42.

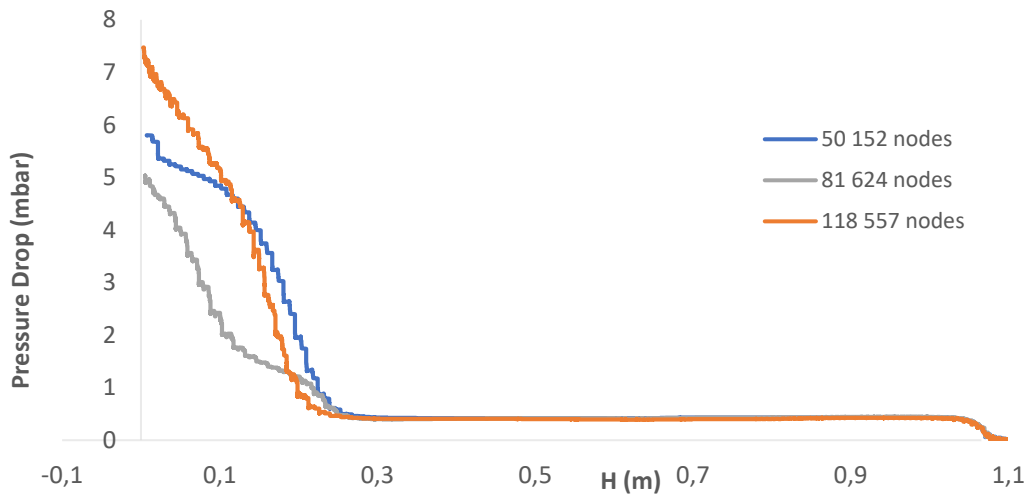


Figure 42- The pressure drop as a function of bed height using different grids in a pilot-scale fluidization unit with a CFD simulation. ($v_g=3.3$ m/s, $t=30$ s)

Figure 42 shows that the pressure drop profile is nearly linear in the bed height, essentially for the mesh with 118 557 nodes, which means that this mesh is effective in describing the pressure drop distribution.

Table 12- Grid analysis shows the mean values of pressure drop for the different meshes, the experimental value, and the errors associated with these values compared to the empirical equation.

Table 12- Grid analysis for pilot-scale fluidization unit with a CFD simulation.

	50 152 nodes	81 624 nodes	118 557 nodes	Experimental data	Classical equation
Pressure drop (mbar)	6.20	6.05	5.91	7	5.89
Error (%)	5.26	2.72	0.34	18.85	-

Considering the nodes number and the different meshes quality present in Table 4- Number of nodes and quality parameters for the pilot-scale fluidization unit meshes is expected that the mesh with the smallest associated errors will be the mesh with 118 557 nodes.

Regarding the experimental pressure drop, this presents a pronounced error quite possibly due to the device that indicates the value. Since the device only indicates the value of the units, the measurement accuracy will be lower. Another reason for the high error may be that the laboratory's pilot-scale fluidization unit is constantly opened, which may affect the measuring sensors.

Considering all sensitivity analysis results explained above is possible to state that the mesh with 118 557 nodes is adequate for the hydrodynamics prediction in the pilot-scale fluidization unit.

C.2. Grid for industrial-scale FBR

The current study focuses on finding a suitable number of cells that are adequate to predict the hydrodynamics in the industrial-scale FBR and provide grid-independent results. In order to validate the model, the simulation results were compared with the theoretical value calculated from equation (1) and (2).

In Table 7, it is possible to see the number of nodes and quality parameters for the industrial-scale reactor meshes.

Using the classical equations (1) and (2), it is possible to calculate the pressure drop. Since that the gas density is higher in this section, compared with the last subchapter, the gas pressure drop component will influence much more, and the gas phase pressure drop will already be considerable.

CFD simulated pressure drop data was compared with the classical calculated data according to the empirical equation, $\Delta P = 0.4153 \text{ bar}$, for a simulation real time of 30 s, as shown in Figure 43.

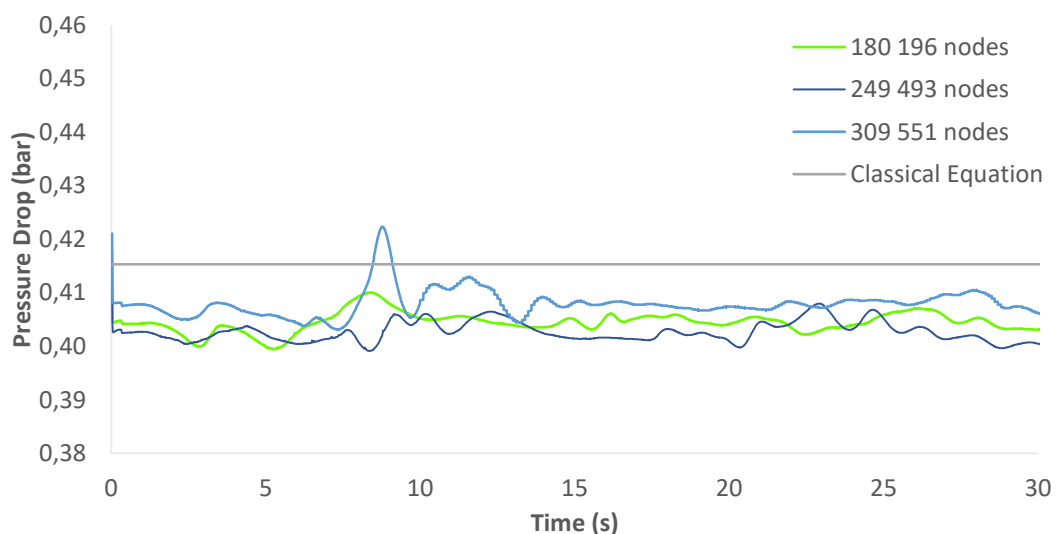


Figure 43- The pressure drop as a function of flow time using different grids in an industrial-scale FBR with a CFD-PBM simulation. ($v_g=0.38 \text{ m/s}$). The theoretical value of 0.4153 bar from classical equations (1) and (2).

To validate the simulation, the results of pressure drop were compared with the theoretical value. The pressure drop profile through the bed is plotted as a function of time and compared to the theoretical value, Figure 43. The simulation results for the three different meshes show small oscillations. However, the results closest to, and around the theoretical value corresponds to the mesh of 309 551 nodes.

Given the simulation conditions, there are not violent motions of particles in the actual bed, so there are not pressure drop values fluctuations.

The pressure drop along the reactor is depicted in Figure 44.

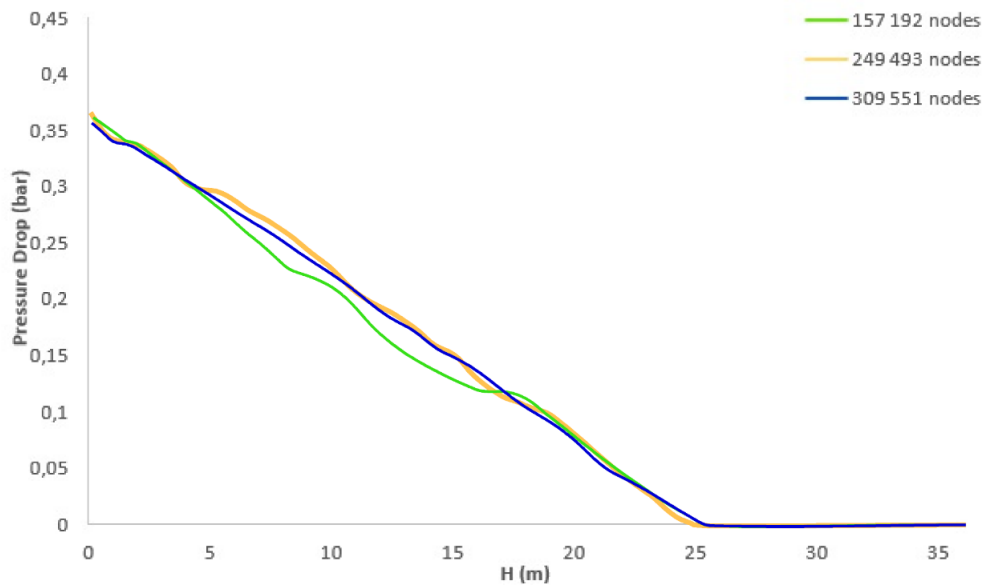


Figure 44- The pressure drop as a function of bed height using different grids in an industrial-scale FBR with a CFD-PBM simulation. ($v_g=0.38$ m/s, $t=50$ s)

Figure 44 shows that the pressure drop profile is nearly linear in the bed height, essentially for the mesh with 118 557 nodes, which means that this mesh is effective in describing the pressure drop distribution.

Table 13 shows the mean values of pressure drop for the different meshes and the errors associated with these values compared to the empirical equation.

Table 13- Grid analysis for industrial-scale

	157 192 nodes	249 493 nodes	309 551 nodes	Classical equation
Pressure drop (bar)	0.4045	0.4032	0.4085	0.4153
Error (%)	2.60	2.92	1.65	-

Considering the nodes number and the different meshes quality present in Table 7 is expected that the mesh with the smallest associated error will be the mesh with 309 551 nodes.

All meshes have a reasonably small error, so grid-independent results would be obtained for all cases. The pressure drop is not sensitive toward the grid resolution. However, and although there was only a 1,3% decrease in the error related to the average pressure drop between the 249 493 nodes and 309 551 nodes mesh, the mesh with more nodes was used since it has a higher quality, and the computational time required to perform the simulation is not excessive.

Considering all sensitivity analysis results explained above is possible to state that the mesh with 309 551 nodes is adequate, and the model can represent the actual behavior of real mixture with reasonable accuracy in terms of pressure drop.

Appendix D – Particle growth rate

The simulation results of an average particle diameter as the simulation times increases in the industrial-scale FBR are shown in Table 14 and Figure 45.

Table 14- Average particle diameter in function of time

Time (s)	Average particle diameter (m)
0	0,0002
10	0,0002102
20	0,0002578
30	0,0002895
40	0,0003139
50	0,0003329
60	0,0003528
70	0,0003600
80	0,0003714
90	0,0003812
100	0,0003898
110	0,0003976
130	0,0004148
150	0,0004526
170	0,0004630
190	0,0005122
200	0,0005163
210	0,000505
230	0,0005381
250	0,0005451

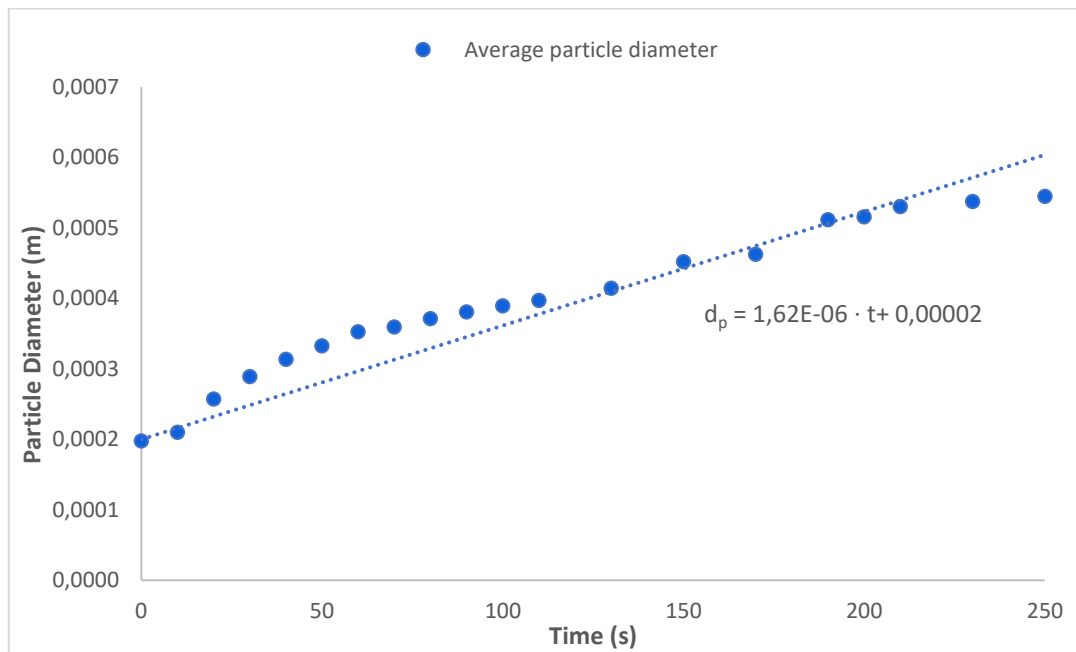


Figure 45-Predicted average particle diameter times profile in the industrial FBR in CFD-PBM simulation.

The slope of Figure 45 represents the growth rate of particles. The mean particle diameter reaches the maximum size of 545.1 μm starting from 200 μm .

The growth rate of particles can be approximated by calculating as follows,

$$G(L_i) = \frac{d(L_i)}{dt} = \frac{0.0005122 - 0.0002}{190 - 0} = 1.62 \cdot 10^{-6} \text{ m/s}$$

Appendix E – User Defined Functions

E.1. User Defined Function for particle growth rate

```
#include "udf.h"
#include "sg_pb.h"
#include "sg_mphase.h"
#include "mem.h"

DEFINE_PB_GROWTH_RATE(growthrate1, cell, thread, d_1)
{
    real kp;
    real Rp;
    real T;
    real Gd;
    real CM;
    real CC;
    real monomer_volume_frac;
    real monomer_density;
    real catalyst_density;
    real catalyst_volume_frac;
        real kop =1.0e06; /*frequency factor of propagation reaction*/
        real Ea = 33500; /*activation energy (J/mol)*/
        real Rgas = 8.314; /*gas constant*/
        real Mw_M = 0.02805;
        real Mw_C = 280.05;
        real dim = 0.00005;/**initial particle diameter*/
        Thread *tc = THREAD_SUPER_THREAD(thread);
        Thread **pt = THREAD_SUB_THREADS(tc);
        Thread *tt = pt[0];/*primary phase thread*/
        Thread *tp = pt[1];/*secondary phase thread*/
        monomer_volume_frac = C_VOF(cell,tt);
        monomer_density = C_R(cell,tt);
        catalyst_volume_frac = C_VOF(cell,tp);
        catalyst_density = C_R(cell,tp);
        CM = monomer_volume_frac*monomer_density/Mw_M; /*concentration
monomer (mol/m^3)*/
        CC = catalyst_volume_frac*catalyst_density/Mw_C; /*concentration
catalyst (mol/m^3)*/
}
```



```

T = C_T(cell,tp); /*Temperature(K)*/
kp = kop*exp(-Ea/(Rgas*T)); /*reaction rate constant(mol*m^-
3/s)*/

Rp = kp*CM*CC; /*polymerization reaction (mo;*m^-3/s)*/
Gd = (Rp*pow(dim,3))/(3*catalyst_density*pow(d_1,2)); /*particle
growth rate (m/s)*/
    if (Gd<0)
        {
            Gd=0.000001;
        }
    if (Gd>0.00125)
        {
            Gd=0.00125;
        }
    return Gd;
}

```

E.2. User Defined Function for polymerization heat

```

#include "udf.h"
#include "sg_pb.h"
#include "sg_mphase.h"
#include "mem.h"

DEFINE_SOURCE(source5,c,t,dS,i)
{
    real R_gas = 8.314; /*gas constant */
    real Ea = 33500; /*activation energy (J/mol) */
    real Temp;
    real kop = 1.0e06; /*frequency factor of propagation reaction */
    real kp;
    real conc_M;
    real conc_C;
    real Rp;
    real delQ;

```

```

real delH = 1e05; /*J/mol */

real MW_M = 28.05/1000; /*Molecular weight monomer */

real MW_C = 280.5; /*Molecular weight catalyst */

Thread *tc = THREAD_SUPER_THREAD(t); /*obtain mixture thread */

Thread **pt = THREAD_SUB_THREADS(tc); /* pointer to sub_threads */

Thread *tp = pt[0]; /*primary phase thread */

Thread *ts = pt[1]; /*secondary phase thread */

/* C_YI(c,tp,0)*C_R(c,tp)/MW_M; C_VOLUME(c,t)*/

conc_M = C_VOF(c,tp)*C_R(c,tp)/MW_M;

/*Message("conc_M: %g\n",conc_M);*/

conc_C = C_VOF(c,ts)*C_R(c,ts)/MW_C;

/*Message("?????????????????: %g\n",C_VOF(c,tc));*/

/*Message("C_VOF(c,t):%g          C_VOF(c,tp):%g          C_VOF(c,ts):
%g\n",C_VOF(c,t),C_VOF(c,tp),C_VOF(c,ts));*/

Temp = C_T(c,t);

kp = kop*exp(-Ea/(R_gas*Temp));

Rp = kp*conc_M*conc_C;

delQ = Rp*delH;

    if (delQ<0.5)
        {
            delQ=0.5;
        }

    if (delQ>100.8)
        {
            delQ = 100.8;
        }

return delQ;
}

```